# Proximal Surface Pedogeophysical Characterization in Maritime Antarctica: Assessing Pedogeomorphological, Periglacial, and Landform Influences

Danilo César de Mello<sup>1</sup>; Clara Glória Oliveira Baldi<sup>1</sup>; Cássio Marques Moquedace<sup>1</sup>; Isabelle de Angeli. Oliveira<sup>1</sup>; Gustavo Vieira Veloso<sup>1</sup>; Lucas Carvalho Gomes<sup>3</sup>; Márcio Rocha Francelino<sup>1</sup>; Carlos Ernesto Gonçalves Reynald Schaefer<sup>1</sup>; Elpídio Inácio Fernandes-Filho<sup>1</sup>; Edgar Batista de Medeiros Júnior<sup>1</sup>; Fabio Soares de Oliveira<sup>4</sup>; José João Lelis Leal de Souza<sup>1</sup>; Tiago Osório Ferreira <sup>2</sup>; José Alexandre Melo Demattê<sup>2</sup>

- <sup>1</sup> Department of Soil Science, Federal University of Viçosa: daniloc.demello@gmail.com; clara.baldi@ufv.br; 0 cassio.moquedace@ufv.br; isabelle.angeli@ufv.br; gustavo.v.veloso@gmail.com; marcio.francelino@ufv.br; carlos.schaefer@ufv.br; elpidio@ufv.br; edgar.junior@ufv.br; jilelis@ufv.br
  - <sup>2</sup> Department of Soil Science, "Luiz de Queiroz" College of Agriculture, University of São Paulo, Av. Pádua Dias, 11, CP 9, Piracicaba, SP 13418-900, Brazil; e-mails; toferreira@usp.br; jamdemat@usp.br
  - <sup>3</sup> Department of Agroecology, Aarhus University, Blichers Allé 20, 8830 Tjele, Denmark: lucas.gomes@agro.au.dk
  - <sup>4</sup> Department of Geography, Federal University of Minas Gerais: fabiosolos@gmail.com

Correspondence to: Danilo César de Mello (daniloc.demello@gmail.com)

**Abstract.** Maritime Antarctica (M.A.) contains the most extensive and diverse lithological exposure compared to the entire continent. This lithological substrate reveals a rich history encompassing lithological, pedogeomorphological, and glaciological aspects of M.A., all of with are influenced by periglacial processes. Although pedogeophysical surveys can detect and provide valuable information to understand Antarctic lithologies and their history, such surveys are scarce on this continent and, in practice, almost non-existent. In this sense, we conducted a pioneering and comprehensive gamma-spectrometric (natural radioactivity) and magnetic susceptibility ( $\kappa$ ) survey on various igneous rocks. This study aimed to improve the geoscientific understanding of periglacial and pedogeomorphological processes in Keller Peninsula by integrating radiometric and magnetic data with advanced spatial analysis. It investigates the spatial variability of natural radiouclides and magnetic susceptibility across different substrates, evaluates a machine learning approach for data modelling, and interprets γ-ray and κ maps to reveal soil and landscape-forming processes. For that, we used proximal gamma-spectrometric and  $\kappa$  data in different lithological substrates associated to terrain attributes. The pedogeophysical variables were collected in the field from various lithological substrates, by use field portable equipment. The pedogeophysical variables were collected in the field from various lithological substrates using portable equipment. These variables, combined with relief data and lithology, served as input data for modeling to predict and spatially map the content of radionuclides and  $\kappa$  by random forest algorithm (RF). In addition, we use nested-LOOCV as a form of external validation in a geophysical data with a small number of samples, and the error maps as evaluation of results. The RF algorithm successfully generated detailed maps of gamma-spectrometric and κ variables. The distribution of radionuclides and ferrimagnetic minerals was influenced by morphometric variables. Nested-LOOCV method

evaluated algorithm performance accurately with limited samples, generating robust mean maps. The highest thorium levels were observed in elevated, flat, and west beach areas, where detrital materials from periglacial erosion came through fluvioglacial channels. Lithology and pedogeomorphological processes-controlled thorium contents. Steeper areas formed a ring with the highest uranium contents, influenced by lithology and geomorphological-periglacial processes (rock cryoclasty, periglacial erosion, and heterogeneous deposition). Felsic rocks and areas less affected by periglacial erosion had the highest potassium levels, while regions with sulfurization-affected pyritized-andesites near fluvioglacial channels showed the lowest potassium contents. Lithology and pedogeochemical processes governed potassium levels. The  $\kappa$  values showed no distinct distribution pattern. Hydrothermal alteration affected the pyritized andesites, with heat and magmatic fluids driving iron enrichment and the formation of hydrothermal magnetite, which in turn led to elevated  $\kappa$  values. Conversely, Cryosol areas, experiencing freezing and thawing activity, had the lowest  $\kappa$  values due to limited ferrimagnetic mineral formation. In regions characterized by diverse terrain attributes and abundant active and intense periglacial processes, the spatial distribution of geophysical variables does not reliably reflect the actual lithological composition of the substrate. The complex interplay of various periglacial processes in the area, along with the morphometric features of the landscape, leads to the redistribution, mixing, and homogenization of surface materials, contributing to the inaccuracies in the predicted-spatialized geophysical variables.

Keywords: machine learning; gamma-ray; magnetic susceptibility; cryopedology

### 1. Introduction

Recently, proximal geophysical sensors have been used for lithological-pedological characterization in other parts of the world, where the provided information is used to understand the lithosphere-pedosphere interaction and dynamics in a geoenvironmental context (Bastos et al., 2023; Vingiani et al., 2022). Pedogeophysics is the application of one or more geophysical survey techniques to pedology to acquire pedogeophysical variables, aiming to understand pedogenesis, soil attributes, their landscape distribution, and the relationships between soil-forming factors and broader land surface processes. Pedogeophysical surveys utilizing sensors enabled the gathering of soil field information swiftly and efficiently, reducing the necessity of sample collection for laboratory analysis (Souza et al., 2021; Mello et al., 2020; Mello et al., 2021; Mello et al., 2023). Among the geophysical techniques used for lithological surveys, radiometric (gamma-ray spectrometry) and magnetic (magnetic susceptibility) stand out.

Gamma-spectrometry involves the quantification uranium (e<sup>238</sup>U), thorium (e<sup>232</sup>Th), and potassium (<sup>40</sup>K) commonly called (radionuclides) in naturally radioactive rocks, soils, and sediments (Minty, 1988). The quantities of these radionuclides are influenced by various factors such as lithological substrate and surface processes (weathering, pedogenesis, geomorphological, and periglacial) (Navas et al., 2018). Dickson and Scott, (1997); Wilford and Minty, (2006) and Mello et al., (2021) have shown that radionuclide contents depend not only on the soil parent material but also on surface processes. Proximal gamma-

65 ray spectrometry offers a precise method for determining concentrations of specific radioactive elements and mapping their sources accurately in soil, bedrock, and surface geological exploration (Ford et al., 2008).

Magnetic susceptibility ( $\kappa$ ) quantifies the degree of magnetization induced in a material relative to the strength of the applied magnetic field (Mullins, 1977). In soils,  $\kappa$  is primarily controlled by ferrimagnetic minerals either inherited from lithological substrates or formed through weathering and pedogenesis, typically occurring as magnetite in the sand fraction and maghemite in the clay fraction (Ayoubi et al., 2018). In addition, the surface processes a role in determining  $\kappa$  values (Garankina et al., 2022; Mello et al., 2020; Ribeiro et al., 2018; Sarmast et al., 2017).

Many studies used gamma-ray spectrometry mapping to delineate lithological maps (Arivazhagan et al., 2022; Loiseau et al., 2020; Shebl et al., 2021) and magnetic susceptibility (Bressan et al., 2020; Costa et al., 2019; Harris and Grunsky, 2015). In addition, recently Mello et al., (2022), Mello et al., (2020), Mello et al., (2021), Mello et al., (2022), Mello et al., (2022) have successfully used machine learning algorithms combined with data from multiple field geophysical equipment to map pedogeophysical variables and understand tropical soils, lithology and landscapes, obtaining satisfactory results in mapping and understanding these landscapes using modeling via machine learning algorithms.

Maritime Antarctica (MA) is currently a great geosciences frontier to be explored in pedogeophysical studies in with its complex and heterogeneous landforms and lithological characteristics. MA has a different climate from continental Antarctica, being hotter and more humid (Turner et al., 2007, 2005). In this region, periglacial environments are abundant and ruled by seasonal cycles of water freezing-thawing, which determine the specific landforms, permafrost and typical soils (French, 2017; Pollard, 2018). The MA lithology is predominantly composed of igneous rocks and a few sedimentary rocks. This complex lithological system associated with climatic conditions produces heterogeneous soils, sediments and saprolites, forming a unique geoenvironment on the planet (Meier et al., 2023; Siqueira et al., 2022).

Traditionally geoscientists use invasive, destructive and time-consuming techniques for lithological and pedological characterization in natural systems, employing sample collection for physical-chemical and mineralogical analysis in the laboratory. Besides, the lack of detailed characterization of samples in the field demands a high collection of samples. In Antarctica, material collection is limited by a lack of logistics and restricted access to a small number of researchers who sample on the continent. While geophysical survey techniques are well-established and commonly utilized in research, only a few studies have demonstrated their use, specifically gamma-ray spectrometry and magnetic susceptibility, for characterizing and understanding periglacial landscapes such as MA (Mello et al., 2022). This scarcity of studies is particularly evident in the Antarctic environment, where hostile and inaccessible conditions have limited pedogeophysical characterization such as gamma spectrometry and magnetic susceptibility mapping, and their correlation with periglacial processes and landforms. Fieldwork logistics in such extreme geoenvironmental settings are inherently challenging. Consequently, acquiring in situ pedogeophysical data can support more accurate inferences about the lithological, mineralogical, and pedological characteristics of the terrain, reducing the need for extensive sample collection and laboratory analysis. This approach is especially valuable when utilizing diverse sensor technologies in remote and sensitive environments.

Given the above, this study aimed to enhance the geoscientific understanding of periglacial and pedogeomorphological processes in Keller Peninsula (Maritime Antarctica) by integrating radiometric and magnetic surficial data with advanced spatial analysis techniques. Specifically, we sought to: i) investigate how natural radioactivity ( $^{238}$ U,  $^{232}$ Th, and  $^{40}$ K) and magnetic susceptibility ( $\kappa$ ) vary across heterogeneous lithological and pedological substrates and how they reflect underlying geomorphic and periglacial dynamics; ii) evaluate the performance of a machine learning algorithm, combined with the Nested Leave-One-Out Cross-Validation method, in modeling and spatializing pedogeophysical surface data; iii) use the generated gamma-ray ternary and  $\kappa$  maps as tools to interpret and reveal spatial patterns related to soil development, rock weathering, and cryogenic processes in the study area.

This study can improve our understanding about periglacial processes, which can improve pedogeophysical surveys and soillithological digital mapping in the Antarctic environment. This expectation is based on research that has focused on comprehending lithological characteristics, periglacial processes and landscape evolution in Antarctic pedosphere-lithosphere interactions.

### 2 Material and methods

100

105

110

115

120

125

130

### 2.1 Study area, lithological-soil surveys and sampling points

The study site comprises Keller Peninsula (62°4′33″ S, 58°23′46″W), Admiralty Bay, King George Island, and in the South Shetland Archipelago in M.A. (**Fig. 1**). The Keller Peninsula covers an area of 500 ha, stretching 4 km (north-south) and 2 km (east-west) (Francelino et al., 2011). The geological framework of Keller Peninsula (Admiralty Bay, King George Island) was characterized based on the volcanic stratigraphy described by Birkenmajer, (1980) and subsequent revisions of the volcanic geology of Admiralty Bay. The peninsula is composed predominantly of Tertiary volcanic sequences, representing three major eruptive cycles associated with caldera collapse and subsequent migration of volcanic centers. Field descriptions and petrographic data indicate the dominance of basaltic-andesitic to andesitic lithologies, locally pyritized, with phenocrysts of labradorite-andesine plagioclase and accessory pyroxenes. These lithological features, combined with the caldera structure and stratigraphic relations to Ullman Spur and Point Hennequin, were used to establish the geological context of the study area, ensuring a robust framework for subsequent soil, geomorphological, and pedogeophysical analyses.

We used the most detailed comprehensive lithological map of Admiralty Bay and its surroundings produced by British geologists stationed at Base G on Keller Peninsula between 1948 and 1980 (Birkenmajer, 1980), at a scale of 1:50,000. The geological framework of the area is linked to volcanic activity involving transitional magmas between the oceanic crust and the Antarctic Plate, generating basaltic to andesitic lavas, pyroclastic deposits, volcanic tuffs, and hypabyssal intrusions, dated from the Upper Cretaceous to the Oligocene (Pride et al., 1990). Overall, the lithology of Keller Peninsula is dominated by igneous rocks, including andesitic-basalts, basaltic-andesites, diorites, pyritized-andesites, and tuffites, as well as undifferentiated Quaternary deposits comprising local material and sediments reworked by marine erosion (Fig. 2A). Marine terraces characterize the lower landscape, while andesitic-basalts and basaltic-andesites predominate in the upper sectors.

Pyritized-andesites occur in various topographic positions, tuffites typically occupy intermediate elevations, and diorites appear sporadically in isolated outcrops. These data supported the interpretation of bedrock as a key soil-forming factor, particularly in the mobilization and spatial distribution of radionuclides (<sup>238</sup>U, <sup>232</sup>Th, and <sup>40</sup>K) in surface soils. The mineralogical composition of the parent material, especially the presence of Fe-bearing silicates and accessory minerals, influenced the geochemical dynamics of secondary ferrimagnetic mineral formation and the inheritance of primary minerals. The spatial relationship between sampling points and lithological boundaries was assessed using a detailed lithological map, revealing distinct geological compartments corresponding to variations in landscape relief.

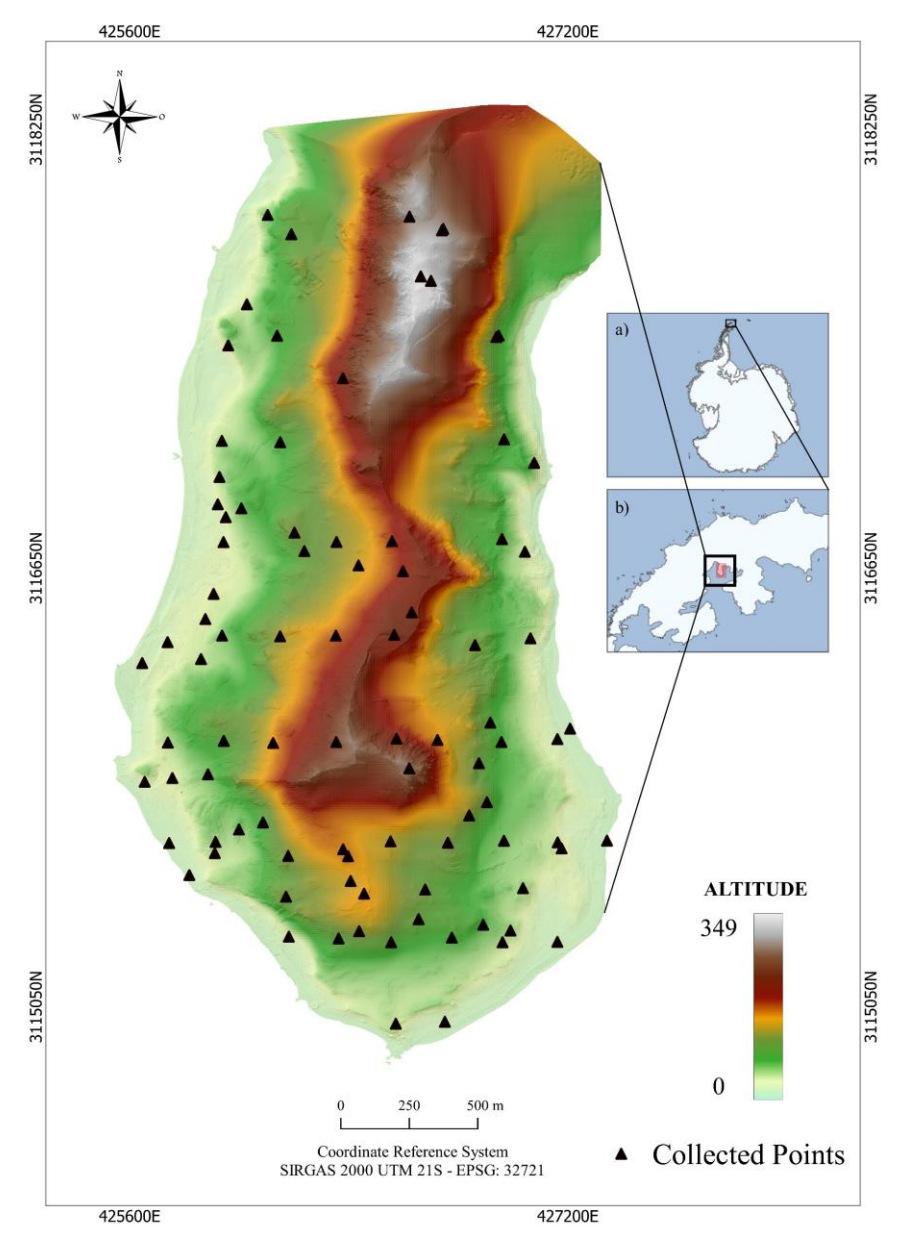




**Figure 1.** Study area in Maritime Antarctic (Keller Peninsula), collected point, digital elevation model, and geophysical sensors. a) Antarctic continent; b) Keller Peninsula. A – Gamma-ray spectrometer (Radiation Solution – RS 230); B – Magnetic susceptibility meter (KT-10 Terraplus); C – Gamma-ray readings; D- Magnetic susceptibility readings.

The weather in Maritime Antarctica follows a typical pattern, albeit slightly warmer, as outlined by Rakusa-Suszczewski et al., (1993). Summer (December–March) temperatures average around +1.6°C, whereas winter (June–September) temperatures drop to an average of -5.3 °C (INPE, 2009). Annual precipitation is around 400 mm. The Keller Peninsula spans elevations between 0 and 380 meters above sea level, featuring a diverse topography from flat to steep (slopes ranging from 0 to 75%). This region is characterized by various landforms like moraines, protalus, inactive rock glaciers, uplifted marine terraces, and Felsenmeer. These lithological features have formed due to both paraglacial and periglacial conditions, as discussed by Francelino et al., (2011).

145

155

The lower portions of the landscape consist mainly of marine terraces. At intermediate elevations, lithified pyroclastic deposits, known as tuffites, are predominant. These tuffites are characterized by volcanic glass shards, plagioclase, and pyroxene crystals, as well as lithic clasts embedded in a fine ash matrix. They frequently exhibit varying degrees of alteration, including chloritization and sericitization, and may be cemented by secondary silica or calcite (Nawrocki et al., 2021).

Above the tuffites, extensive outcrops of andesitic-basalts and basaltic-andesites dominate the upper landscape. These volcanic rocks primarily consist of labradorite-andesine phenocrysts set within a groundmass of plagioclase, volcanic glass, and clinopyroxene (Nawrocki et al., 2021). Scattered throughout these units are occurrences of pyritized andesites, which have undergone significant post-magmatic hydrothermal alteration. This alteration transformed primary plagioclase and pyroxene into secondary minerals such as chlorite, albite, carbonate, and quartz. Additionally, quartz–pyrite mineralization developed within these andesites (Birkenmajer, 1980).

Less abundant and restricted to specific localized zones, diorite outcrops occur notably on Keller Peninsula. These diorites are composed mainly of plagioclase (andesine to labradorite), hornblende, and minor biotite, with accessory minerals such as magnetite, apatite, titanite, and zircon. The texture is generally coarse-grained and equigranular (Birkenmajer, 1980; Valeriano et al., 2008).

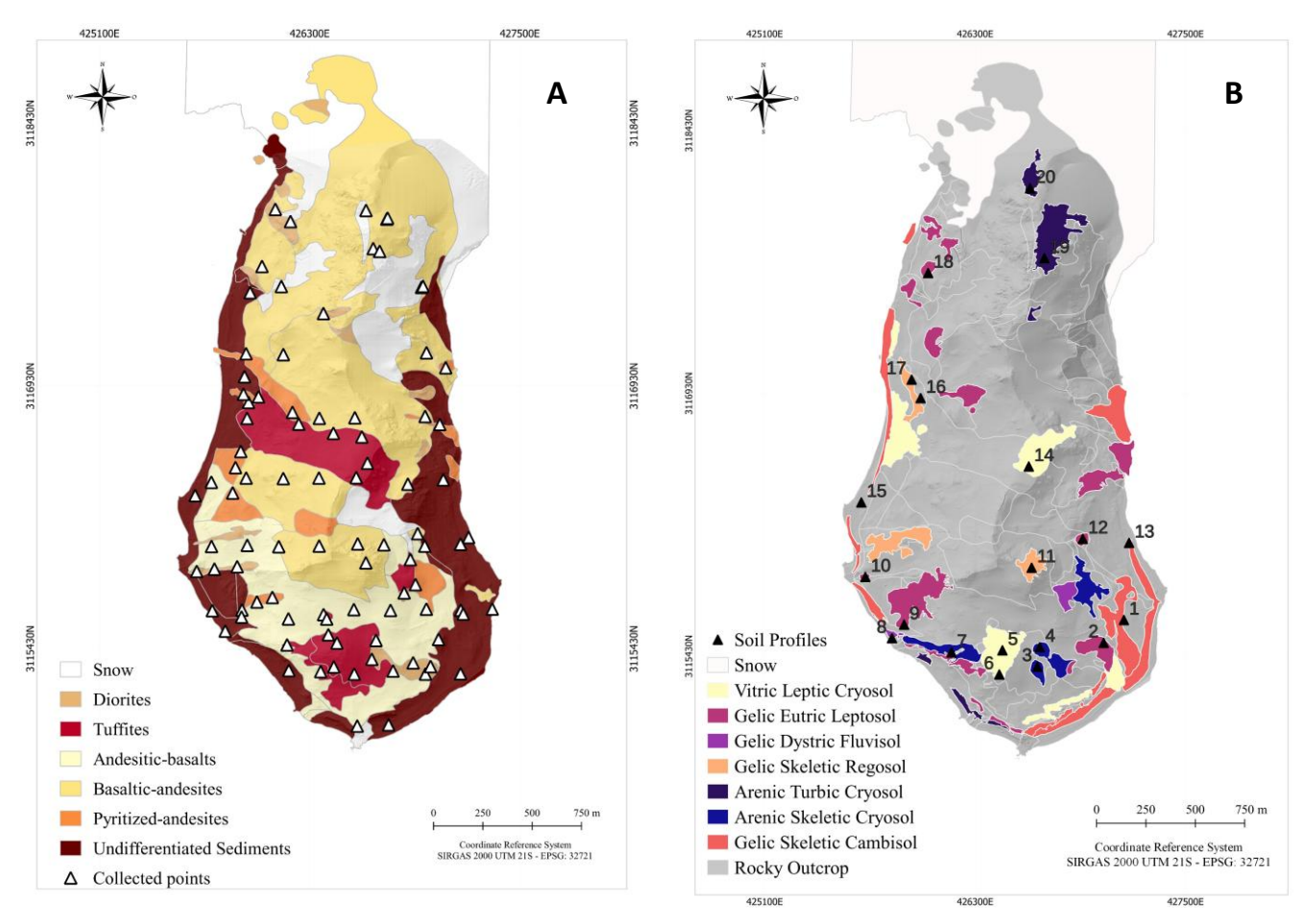


**Figure 2**. The maps indicated: A) Lithology (adapted from Birkenmajer, 1980). B) Soil classes: The lithological and soil classes maps were adapted from Francelino et al., (2011).

Soil classification and mapping were carried out by an experienced pedologist, using 20 representative soil profiles. The overall soil development in the area is limited, and according to the World Reference Base for Soil Resources (WRB) (FAO, 2014), 2014), the soils in the region can be categorized into various types, including Gelic Eutric Leptosol, Gelic Skeletic Regosol, Gelic Skeletic Cambisol, Gelic Leptic Regosol, Gelic Dystric Fluvisol, Arenic Skeletic Cryosol, Vitric Leptic Cryosol, Gelic Leptic Cambisol, and Arenic Turbic Cryosol, as illustrated in Figure 2B. The occurrence of permafrost was observed the first two meters below the soil surface in five soil profiles. Additionally, it is discontinuously found within the first two meters in regions with mid-slope and flat topography, all of which are classified as Cryosols (Francelino et al., 2011; Mello et al., 2023). Within each soil profile, samples were meticulously collected from identified diagnostic soil horizons at various soil depths to facilitate subsequent physico-chemical analyses.

The sampling design and the selection of measurement locations were conducted while considering mainly 5 topossequences (topographic gradients) that account for various lithologies and soils. The distribution of collection points by the proximal gamma-ray and magnetic susceptibilimeter is shown in **figure 1**. The readings with the sensors were carried out, taking into account the lithological diversity of the Peninsula, as well as pedological diversity and variations in relief.

### 2.2 Pedogeophysical survey, radiometric and κ characterization

180

185

190

195

210

The pedogeophysical variables (radiometric and  $\kappa$ ), were collected using proximal geophysical sensors, RS-230 and KT-10 Terraplus, respectively (Figs. 1A and B, respectively). The radiometric data (gamma-ray spectrometry) correspond to the acquisition of radionuclide contents eU, eTh and  $^{40}$ K, quantified in ppm (eU and eTh) and  $^{6}$  for  $^{40}$ K. Magnetic susceptibility is given in  $10^{-3}$  SI units and the sensor is able to detect mean  $\kappa$  values to a depth of 2 cm below the rock outcrops surface (Sales, 2021). Detailed calibration methods, method of collection and interpretation of results can be found in (Mello et al., 2022; Mello et al., 2021, 2022).

Gamma spectrometric readings (**Fig. 1 C**) were taken on the rock outcrop surface and soil depth (saprolite/rock), at the 91 collection points shown in figure 1, in "essay mode", which provides greater precision, and the reading time was adjusted to 3 minutes at each point. The sensor is able to detect radiation up to a mean depth of 30 - 60cm depending on the characteristics of the substrate (Beamish, 2015; Taylor et al., 2002; Wilford et al., 1997a). Subsequently, the equipment data were transferred to a computer and concatenated with soil κ values and environmental data (lithology and terrain attributes).

Similarly, the  $\kappa$  survey readings (**Fig. 1 D**) was undertaken at each of the 87 points to a mean depth of 2 cm below the rock outcrops surface and soil depth (saprolite/rock). Three readings were taken for each point to reduce sensor noise and increase the precision reading and, the  $\kappa$  mean values of these three readings were used in data processing. The resulting  $\kappa$  data were then combined with their respective gamma-ray spectrometric data, lithology and terrain attributes in order to be processed. All readings were carried out in different lithological-pedological compartments, with emphasis on in situ materials (igneous rocks), despite of the little presence of marine terraces with presence of external materials.

It is important to highlight that only 87 points with geophysical sensors were taken on pedological substrates. Furthermore, these few points are found in soils with little pedogenetic evolution, characterized by a high content of rock fragments and a predominance of the coarse fraction composed of cryoclastic rocks (many with a skeletal character). Additionally, where there was soil, we opened a small trench and carried out geophysical readings at the base of the soil profiles, in direct contact with the rock. As a result, we do not have enough number of points to carry out an analysis to identify differences between surface geophysical variables and pedological substrates. Therefore, we consider these points as readings carried out on the lithological substrate.

### 2.3 Digital Elevation Model

Geoprocessing and Digital Elevation Model (DEM) analysis were conducted utilizing R software version 4.10 version (R Core Team, 2023), employing data derived from a High-Resolution Topography (HRT) survey to create the DEM (**Fig. 1**). The

HRT survey, conducted during the 2014/2015 and 2015/2016 periods, utilized a Terrestrial Laser Scanner (TLS) of the RIEGL VZ-1000 model, known for its nominal accuracy and precision of 8 and 5 mm, respectively (Schünemann et al., 2018). This advanced sensor and geoprocessing methodology yielded a low root mean square error and a high number of points per cell, resulting in a densely populated point cloud. This dataset facilitated a comprehensive generalization process to generate surface models with superior performance, accurately representing local relief. This, in turn, enabled in-depth studies of landscape evolution at a micro scale over time, specifically allowing for the assessment of pedogeomorphological processes.

Using the R software (R Core Team, 2023), a total of forty-eight additional topographic attributes were computed based on the DEM data extracted from the Digital Terrain Model (DTM) (**Table 1**). These attributes were derived using the utilization of the "Rsaga" tool (Brenning, 2008) and the "raster" package (Hijmans and Van Etten, 2016).

220

**Table 1.** Terrain attributes generated from the digital terrain model, geology, soil and spectral indices.

Terrain attributes, geology and spectral indices	Abbreviations	Brief description	
Aspect	AS	Slope orientation	
Blue Band	В	The blue band wavelengths fall below 1546.12 nm.	
Green Band	G	BA primary wavelength of 495-570 nm approximately	
Red Band	R	The longer wavelengths of 1546.12 nm and higher	
Curvature classification	CC	Curvature classification	
Convergence index	CI	terrain parameter which shows the structure of the relief as a set of convergent areas (channels) and divergent areas (ridges).	
Difference	D	Geometric difference of the overlayed polygon layers	
Diurnal anisotropic heating	DAH	Continuous measurement of exposure-dependent energy	
Easterners	EA	Degree of orientation of a slope toward the east	
Flow Line Curvature	FLC	Represents the projection of a gradient line onto a horizontal plane	
General curvature	GC	The combination of both plan and profile curvatures	
Lithology	GEO	Rocks and similar substances that make up the earth's surface	
Hill shade	НІ	A technique where a lighting effect is added to a map based on elevation variations within the landscape.	
Digital elevation model	DEM	Representation of the bare ground (bare earth) topographic surface of the Earth excluding trees, buildings etc.	
Effective air flow heights	EAFH	A line representing the resultant velocity of the disturbed airflow	
Longitudinal curvature	LC	Measures the curvature in the downslope direction	

Terrain attributes, geology and spectral indices	Abbreviations	Brief description  Multivariate distance methods for geomorphographic relief classification	
Mass balance index	MBI		
Maximal curvature	MAXC	Maximum curvature in the local normal section	
Mid-slope position	MSP	Represents the distance from the top to the valley, ranging from 0 to 1	
Minimal curvature	MINC	Minimum curvature for the local normal section	
Morphometric Protection Index	MPI	Measure of exposure/protection of a point from the surrounding relief	
Multiresolution index of ridge top flatness	MRRTF	Indicates flat positions in high-altitude areas	
Multiresolution index of valley bottom flatness	MRVBF	Indicates flat surfaces at the bottom of valley	
Normalized Difference Vegetation Index	NDVI	Remote sensing techniques used to assess the health and densit vegetation.	
Normalized height	NH	Vertical distance between base and ridge of normalized slope	
Northerns	NO	Means in or from the north of a region	
Ridge level	RL	The maximum vertical distance between the finished floor level and the finished roof height directly above.	
Slope	S	Represents local angular slope	
Slope height	SH	Vertical distance between the base and the ridge of slope	
Slope Index	SI	Represents the local angular slope index	
Solrad Diffuse1	SolDiffuse1	Diffuse insolation for the month of January	
Solrad Diffuse2	SolDiffuse2	Diffuse insolation for the month of July	
Solar total radiation	SolTR	Insolation duration for the month of January	
Solrad Direct1	SolDiret1	Direct insolation for the month of January	
Solrad Direct2	SolDiret2	Direct insolation for the month of July	
Solrad Ration1	SolRation1	Ratio between direct insolation and diffuse insolation for the month of January	
Solrad Ration2	SolRation2	Ratio between direct insolation and diffuse insolation for the month of July	
Soil	S	Soil body as triphasic system	
Sky view factor	SVF	Defines the ratio of sky hemisphere visible from the ground	

Terrain attributes, geology and spectral indices	Abbreviations	Brief description  Vertical distance between base and standardized slope index	
Standardized height	STANH		
Tangential curvature	TANC	Measured in the normal plane in a direction perpendicular to the gradient	
Terrain ruggedness index	TRI	Quantitative index of topography heterogeneity	
Terrain surface convexity	TSC	Ratio of the number of cells that have positive curvature to the number of all valid cells within a specified search radius	
Terrain surface texture	TST	Splits surface texture into 8, 12, or 16 classes	
<b>Total curvature</b>	TC	General measure of surface curvature	
Total insolation	TSR	The amount of solar energy that strikes a given area over a specific time,	
Topographic openness	ТО	Expresses the dominance (positive) or enclosure (negative) of a landscape location.	
Topographic position index	TPI	Difference between a point's elevation and surrounding elevation	
Valley depth	VD	Calculation of vertical distance at drainage base level	
Valley	VA	Calculation of fuzzy valley using the Top Hat approach	
Valley Index	VA	Calculation of fuzzy valley index using the Top Hat approach	
Vector ruggedness index	VRI	Measure terrain ruggedness as the variation in three-dimensional orientation	
Topographic wetness index	TWI	Describes the tendency of each cell to accumulate water as a function of relief	
Wind exposition	WE	The average of wind effect index for all directions using an angular step	

### 2.4 Modeling processes and statistical analysis

225

230

The point values of eU, eTh,  $K^{40}$ , and  $\kappa$ , linked with terrain attributes, soil type, lithology, and RGB (**Table 1**), were utilized to modeling these variables for other areas, employing the Random Forest (RF) algorithm. The modeling process comprises two main steps: covariate selection and model tuning / performance evaluation. During the covariates the selection phase, the algorithm aims to generate an optimal set of covariates, adhering to the principle of parsimony. This involved two sequential methods, we initially removed self-correlated variables and subsequently assessed the importance of the remaining variables. Initially, to assess the correlation between variables, we used a Spearman correlation cut-off limit > |0.95|. We eliminated one variable from each pair showing correlations above the established threshold. To decide which variable to remove, we selected the one with the highest sum of absolute correlations with the remaining covariates in the dataset. To carry out this phase, we employed the "cor" and "findcorrelation" functions from the "stats" (Hothorn, 2021) and "caret" (Kuhn et al., 2020) packages

in the R software, respectively (Kuhn and Johnson, 2013). The covariates that successfully passed this selection phase were combined with the samples and, subsequently, the samples were separated into training and test sets.

To partition the data into training and test subsets, we adopted the "nested leave-one-out cross-validation" (nested LOOCV) method (Ferreira et al., 2021; Paes et al., 2022; Rytky et al., 2020). It is noteworthy that the number of samples and readings obtained from geophysical sensors was limited (92) due to various challenges encountered during data collection in the field (e.g., sloping terrain, high hazard areas, glaciers, steep terrain, snowbanks, etc.). Given the small sample size, the nested LOOCV method was chosen, as this method has already been recommended by other authors in similar cases (Ferreira et al., 2021; Mello et al., 2022a; Mello et al., 2022c, 2022b). This particular approach represents a significant innovation in our research.

The nested LOOCV approach involves a double looping process. In the first loop, the model is trained on a dataset of size n-1, and in the second loop, testing is performed using the omitted sample to evaluate the training performance (Jung et al., 2020; Neogi and Dauwels, 2019; Mello et al., 2025). The final machine learning algorithm performance results are calculated as average performance indicators across all points (training/testing). This method proves to be robust in evaluating the real generalization ability of the algorithm and in identifying possible problematic samples or outliers in the data set. Each iteration generates a training set that undergoes covariate selection by importance and subsequent training.

245

250

255

260

The covariate selection based on importance is executed using the backward-forward method, employing the Recursive Feature Elimination (RFE) function available in the "caret" package (Kuhn and Johnson, 2013). This RFE technique is algorithm-specific and yields an optimal set of covariates utilized in predicting the final model for each respective algorithm (Moquedace et al., 2024). RFE is a selection procedure that iteratively removes variables contributing the least to the model, employing an importance measure tailored to each algorithm (Kuhn and Johnson, 2013).

The algorithm is then trained on discrete subsets of variables, going from 2 to the total variables one by one. The ideal subset of covariates is optimized based on the leave-one-out cross-validation (LOOCV), for each of the internal hyperparameters of the tested algorithms (10). The hyperparameters for each algorithm are described in the caret package manual, Chapter 6, "Described Models", available at https://topepo.github.io/caret/train-models-by-tag.html. The Mean Absolute Error (MAE) was used as a metric to select the best subset for the RF algorithm.

Training is then performed using the previously selected variables and tested with LOOCV. Additionally, ten values of each RF hyperparameter were evaluated. At the end of the training phase, predictions are made on samples not used in the training process, and the results are saved for performance analysis. The assessment of algorithm predictions and sensor sets is carried out using a collection of samples from the outer loop within the nested Leave-One-Out Cross-Validation (LOOCV) method. Three key evaluation parameters are utilized: Concordance Correlation Coefficient (CCC) (Eq. (1)), Root Mean Square Error (RMSE) (Eq. (2)), and Mean Absolute Error (MAE) (Eq. (3)) (Lin, 1989).

$$\rho_{c} = \frac{2p\sigma_{x}\sigma_{y}}{\sigma_{x}^{2} + \sigma_{y}^{2} + \left(\mu_{x} - \mu_{y}\right)^{2}} \tag{1}$$

Where:

265 n represents the number of samples;

ρc is the correlation coefficient between the two variables;

μx and μy are the means for the two variables;

" $\sigma$ " \_"x" ^"2" and " $\sigma$ " \_"y" ^"2" are the corresponding variances;

Pi and Oi represent the predicted and observed values at location i.

270

280

285

290

$$RMSE = \sqrt{\frac{1}{n} \times \sum (Qobs - Qpred)^2}$$
 (2)

$$MAE = \frac{1}{n} \times \sum |Qpred - Qobs|$$
 (3)

Where:

Qpred = the mean of the training samples

275 Qobsi = the validation sample

n =number of samples (loop).

As additional validation, we used the "null model" approach (NULL\_RMSE and NULL\_MAE). This null model involves using the mean value determined from the collected samples (EQ. 4 and EQ. 5). The null model represents the simplest possible model when given a training set, providing a single average value for numerical results.

The null model serves as a reference and can be seen as the simplest adjustable model. Any other models that present similar or inferior performances in relation to the null model must be discarded. This indicates that the final model outperforms the use of average values, highlighting its superior quality in model creation. Furthermore, the null model approach is widely employed, especially in spatialization processes such as kriging, where the variable under consideration exhibits spatial dependence, often called the pure nugget effect. The equations used for NULL\_RMSE and NULL\_MAE calculations are as follows:

$$NULL\_RMSE = \left[\frac{1}{N}\sum_{i=1}^{N} (\overline{Qtrain}_i - Qobs_i)^2\right]^{\frac{1}{2}}$$
 (Eq.4)

$$NULL\_MAE = \frac{1}{n} \times \sum |\overline{Qtrain}_i - Qobs_i|$$
 (Eq.5)

Where:

Otrain = the mean of the training samples

Qobsi = the validation sample

295 n =number of samples (loop).

300

305

310

315

320

325

The NULL\_RMSE and NULL\_MAE values were computed using the nullMode function within the caret package (Kuhn et al., 2020). To assess the overall performance of the algorithms for each attribute, a total of 87 loops were conducted. The training results represent the average performance, and the test sample results were calculated from the 87 outer loops using Equations 1, 2, and 3.

Eighty-seven maps were predicted, yielding one map for each execution of the outer loop in the nested Leave-One-Out Cross-Validation (LOOCV). Coefficient of Variation (CV) was calculated for each pixel across the 87 stacked maps. Additionally, a coefficient of variation map (CV% = standard deviation / mean) was generated to illustrate the variation of predicted values in each pixel of the map relative to the mean. Spatial predictions exhibiting lower CV indicate more consistent results, thereby resulting in smaller errors in the estimation/predictions and reduced uncertainty.

The statistical differences between the pedogeophysical variables and lithology substrates were analysed by using the Kruskal-Wallis and Dunn's posthoc tests with a significance level of 5%.

# 3 Results and discussion

## 3.1. Model's performance and variables' importance

The Random Forest (RF) algorithm was employed to predict gamma-ray data and magnetic susceptibility of the substrate, enabling the production of ternary gamma-ray and κ maps (Table 2). The Concordance Correlation Coefficient (CCC) values ranged from 0.771 to 0.851 (**Table 2**). The CCC is a modified version of the coefficient of determination (R²); in addition to measuring the strength of correlation, it also assesses how closely the model predictions align with the 1:1 line (a 45-degree line from the origin). This feature makes the CCC a robust metric for evaluating both the precision and accuracy of predictions (Svensson et al., 2022; Zhao et al., 2022). Unlike the Pearson correlation coefficient, the CCC can detect systematic bias in model outputs. This key distinction makes it a more appropriate choice for model validation than R² (Khaledian and Miller, 2020). In recent geoscience studies, CCC has been effectively used to assess the performance of machine learning algorithms (Chen et al., 2019; S. Chen et al., 2019; Feng et al., 2019; Khosravi et al., 2018; Mishra et al., 2022; Siqueira et al., 2023; Zhou et al., 2022). In addition, the nested-LOOCV methodological framework was better than NULL-model (**Table 2**), for prediction of radionuclides and magnetic susceptibility with a limited number of samples. This approach consistently generated comparable maps across loops, where 87 samples were utilized for training in each loop, and at the conclusion of the process, all samples were used as the test dataset. As a result, the models and/or coefficients of variation in the maps were similar (Ferreira et al., 2020).

**Table 2.** Model's performance in terms of Concordance Correlation Coefficient (CCC), Root Mean Squared Error (RMSE), Mean Absolute Error (MAE), *NULL RMSE* and *NULL MAE*.

Parameters of		RF Algorithm			
model's performance	eU	eTh	<sup>40</sup> K	κ	
CCC	0.771	0.851	0.817	0.809	
MAE	0.496	1.784	0.497	11.898	
<i>RMSE</i>	0.680	2.432	0.646	15.469	
NULL_RMSE	0.652	2.457	0.502	12.224	
NULL_MAE	0.463	1.818	0.502	15.651	

The importance of covariates in predicting pedogeophysical variables revealed that morphometric attributes such as minimal curvature (MINC), mid-slope position (MSP), diurnal anisotropic heating (DAH), difference (D), total insolation (TSR), flow line curvature (FLC), effective air flow heights (EAFH), terrain surface convexity (TSC), hill shading (HI), aspect (AS), mass balance index (MBI), ridge level (RL), digital elevation model (DEM) minimal curvature (MINC), and convergence index (CI) were the most influential, collectively contributing to over 50% of the reduction in mean prediction error (Fig. 3). In contrast, lithological variables contributed less significantly, accounting for less than 50% of the predictive importance (Fig. 3). Similar results were reported by Cracknell and Reading (2014), Harris and Grunsky (2015), and Kuhn et al. (2018), who also achieved satisfactory performance using the RF algorithm to predict radionuclide content and magnetic susceptibility for lithological mapping. In addition, the Red Band (R) and Green Band (G) were found to be important for predicting <sup>40</sup>K concentrations in more than 75% (Fig. 3). In periglacial Antarctic environments characterized by shallow soils, rugged terrain, sparse vegetation, and exposures of mafic and felsic igneous rocks (Francelino et al., 2011), VIS-NIR reflectance predominantly captures variations in surface mineralogy and soil exposure. Landscape dynamics such as erosion and deposition are largely controlled by relief (Viscarra Rossel, 2011). At our study site, exposed mineral surfaces on steep slopes and weathered areas exhibit strong red band reflectance, making this spectral band a valuable proxy for modelling the spatial distribution of <sup>40</sup>K when integrated with topographic and lithological data within machine learning frameworks.

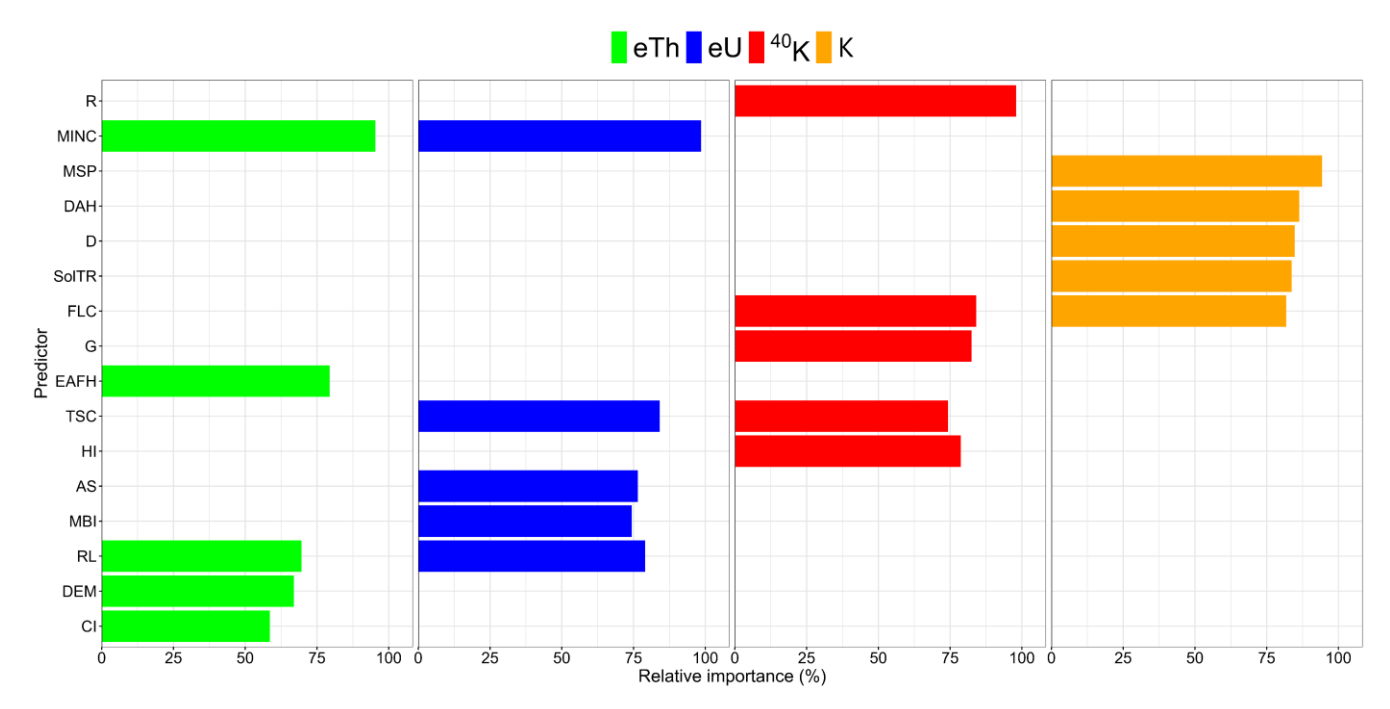


Figure 3. Importance of variables of predictors. *X* axis: variables that most contributed to the predictive models. Axis *y*: value in relative percentage of the contribution. eTh: equivalent thorium; eU: equivalent uranium; <sup>40</sup>K potassium; κ: magnetic susceptibility; The predictors included in the analysis were: Red Band (R); Minimal curvature (MINC); Mid-slope position (MSP); Diurnal anisotropic heating (DAH); Difference (D); Solar total radiation (SolTR); Flow line curvature (FLC); Green Band (G); Effective air flow heights (EAFH); Terrain surface convexity (TSC); Hill shade (HI); Aspect (AS); Mass balance index (MBI); Ridge level (RL); Digital elevation model (DEM); and Convergence index (CI). Colours represent the target variable: green for eTh, blue for eU, red for <sup>40</sup>K, and orange for κ.

# 3.2 Radionuclides and κ contents on lithological compartments and their relationship with mineralogy

355

360

The eU mean content was generally low and showed the greatest variation on the lithologies (**Fig. 4**). The highest eU mean content values were observed on tuffites and the lowest on andesitic-basalts (**Fig. 4**). The diorite presented the highest mean eTh contents, while the andesitic-basalts showed the lowest one. Regarding the  $^{40}$ K, the mean values were high in all lithologies (> 1%) excepted on pyritized-andesite (**Fig. 4**). However, the observed  $^{40}$ K were low compared to those of continental crust rocks (plutonic, metamorphic and sedimentary. According to literature these values are consistent with the average of oceanic crust rocks, which are predominantly basaltic. The highest  $^{40}$ K contents were observed on diorite, and the lowest one on pyritized-andesite (**Fig. 4**). The mean  $\kappa$  values ranged from moderate to low in all lithologies, where pyritized-andesites showed the highest mean values and tuffites the lowest (**Fig. 4**). The descriptive statistics for radionuclides and  $\kappa$  content for all

lithological units are shown in **table 3**, and corroborates and complements the information provided in figure 4 in quantitative terms.

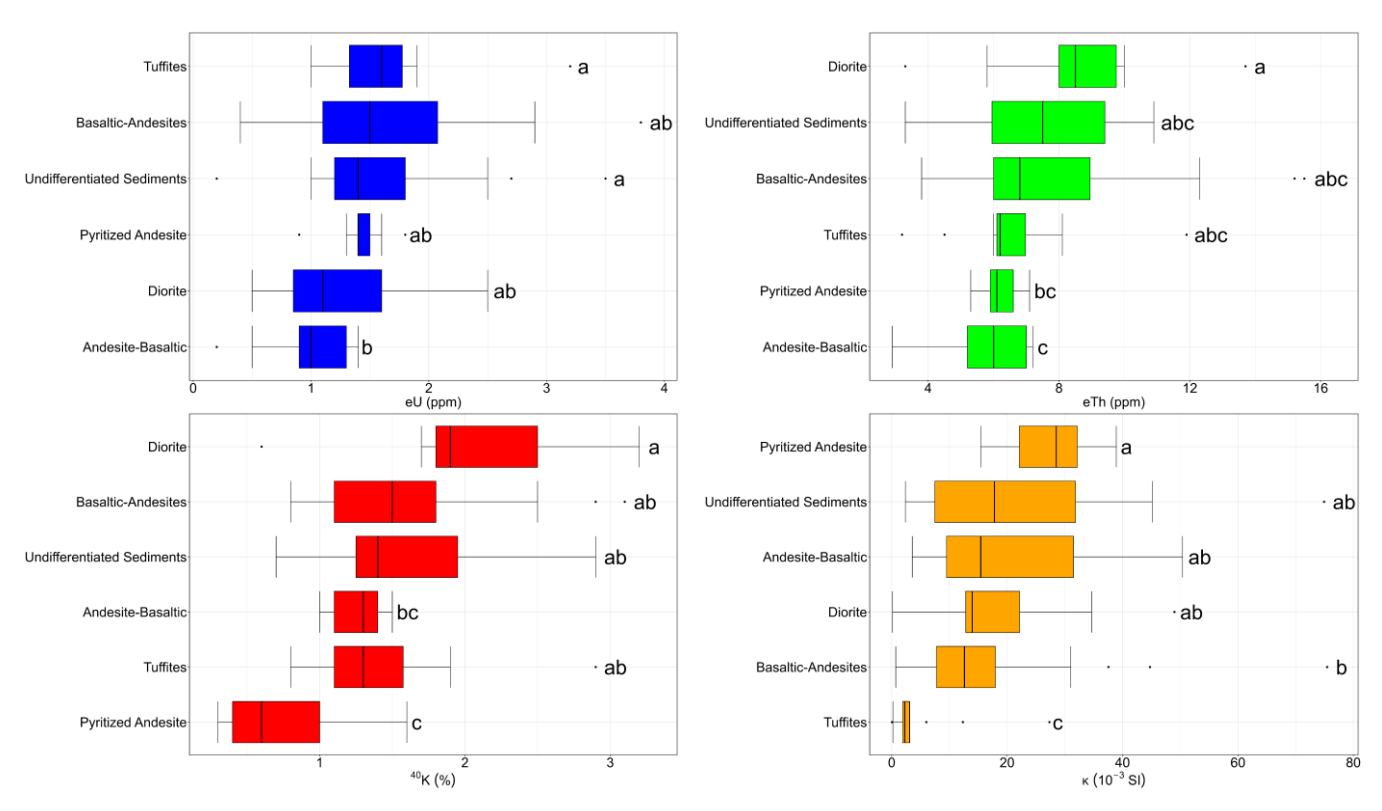


**Figure 4.** *Boxplot* with descriptive statistics of the distribution of radionuclide contents and magnetic susceptibility by lithology. Lowercase letters to the right of the boxplot bars indicate statistical differences as determined by the Kruskal-Walli's test.

Table 3. Descriptive statistics for the analyzed radionuclides and  $\kappa$  by lithology

365

Maximum

	Diorites					
		Radiometric and n	agnetic suscepti	bility		
Summary Statistics	eU(mg.kg <sup>-1</sup> )	eTh(mg.kg <sup>-1</sup> )	<sup>40</sup> K(%)	к (10 <sup>-3</sup> SI units)		
Mean	1.27	8.85	2.10	18.54		
Standard deviation	0.62	3.01	0.74	13.72		
Minimum	0.50	3.30	0.60	0.13		
Maximum	2.50	13.7	3.20	49.0		
	Tuffites					
		Radiometric and magnetic susceptibility				
Summary Statistics	eU(mg.kg-1)	eTh(mg.kg <sup>-1</sup> )	<sup>40</sup> K(%)	к (10 <sup>-3</sup> SI units)		
Mean	1.63	6.62	1.41	4.73		
Standard deviation	0.55	1.96	0.53	7.18		
Minimum	1.00	3.20	0.80	0.04		
Maximum	3.20	11.9	2.90	27.33		
	Andesitic-basalt	ts .				
		Radiometric and magnetic susceptibility				
Summary Statistics	eU(mg.kg <sup>-1</sup> )	eTh(mg.kg <sup>-1</sup> )	<sup>40</sup> K(%)	к (10 <sup>-3</sup> SI units,		
Mean	0.99	5.72	1.26	21.0		
Standard deviation	0.41	1.44	0.17	15.0		
Minimum	0.20	2.90	1.00	3.56		
Maximum	1.40	7.20	1.50	50.4		
	Basaltic-andesite	es				
G G. diedien	Radiometric and magnetic susceptibility					
Summary Statistics	eU(mg.kg <sup>-1</sup> )	eTh(mg.kg <sup>-1</sup> )	<sup>40</sup> K(%)	к (10 <sup>-3</sup> SI units)		
Mean	1.62	7.87	1.59	17.2		
Standard deviation	0.82	3.08	0.61	16.6		
Minimum	0.40	3.80	0.80	0.70		
Maximum	3.80	15.5	3.10	75.4		
	Pyritized-andesit	es				
Commence of the start of	Radiometric and magnetic susceptibility					
Summary Statistics	eU(mg.kg <sup>-1</sup> )	eTh(mg.kg <sup>-1</sup> )	<sup>40</sup> K(%)	к (10 <sup>-3</sup> SI units		
Mean	1.64	7.59	1.54	22.5		
Standard deviation	0.74	2.23	0.57	18.6		
Minimum	0.20	3.30	0.70	2.37		

3.50

10.9

2.90

74.9

In our study area, the high variability in eU content and/or the relatively low concentrations observed in basic—intermediate igneous rocks (Fig. 4, Table 3) can be primarily explained by the fact that uranium and other radionuclides are typically concentrated during the late stages of magmatic crystallization. As a result, mafic rocks, which crystallize earlier in the magmatic sequence, are expected to exhibit lower radionuclide contents (Ragland et al., 1967; Whitfield et al., 1959). In addition, according to Wilford and Minty, (2006) and Wilford et al., (1997b), the mean contents of radionuclides in the Earth crust vary to 2.3%, 3 ppm and 12 ppm, for <sup>40</sup>K, uranium and thorium, respectively, similar to the values observed in our study site.

The eTh and <sup>40</sup>K contents tended to increase with an increase in the silicon content in our lithology composed by igneous rocks (from andesitic-basalts to diorite) (**Fig. 4, table 3**). Our results are corroborated by Dickson and Scott, (1997) and Mello et al., (2023b), who found an increasing in eTh and <sup>40</sup>K contents in acid-felsic igneous rocks and lower levels in basic-mafic igneous rocks. It is noteworthy that the undifferentiated sediments receive materials from various parts of the Peninsula and from outside it, in which case it is not appropriate to use this lithology for radionuclides comparison purposes. Most of the gammaray radiation detected and quantified by the sensor originates from the first 45-60cm of the dry substrate (rocks, soils and sediments), which the mineralogy and geochemistry of the substrate presented the greater contribution to radionuclides contents (Gregory and Horwood, 1961). In addition, Earth surface processes and landforms such as chemical weathering, pedogenesis and relief affect radionuclide contents, since <sup>40</sup>K content decreases with weathering advance once it is removed by destruction of feldspars. Also, <sup>40</sup>K is not incorporated in secondary minerals, so it is leached, whereas Th composes highly resistant minerals, such as ilmenite and zircon. Consequently, Th content increases with weathering (Dickson and Scott, 1997; Wilford et al., 1997b; Mello et al., 2021; Mello et al., 2022; Mello et al., 2023). Despite this, physical weathering in this environment associated with periglacial processes (governed by cycles of freezing and thawing of water in the different portions and types of substrates) should not be neglected, since during these processes, radionuclides are redistributed in the landscape.

The low mean  $\kappa$  values were not expected on basic mafic igneous lithologies (basaltic-andesite, andesitic-basalts) (**Fig. 4, table 3**), since there is a great probability to these rocks present more abundance of ferrimagnetic minerals in the rock. According to Mullins (1977) increasing in ferrimagnetic mineral contents in the substrate results in increases in  $\kappa$  values. The relatively low  $\kappa$  values in the basaltic-andesite and andesitic-basalt substrates may be attributed to the combined influence of the Antarctic cold climate, limited water availability, and slow pedogenesis, which favor the formation of amorphous or poorly crystalline iron oxides, even in lithological substrates with sufficient iron content, such as ferrihydrite, rather than well-crystalline magnetite or maghemite. Despite this,  $\kappa$  values remains highly heterogeneous, except for the tuffites, no statistically significant differences were observed among the other lithologies, including the marine terraces. Regarding the low  $\kappa$  values on tuffite, this igneous rock is formed from volcanic ashes and containing large amounts of poorly crystalline minerals (Fabris et al., 1995), which is difficult to form ferrimagnetic minerals. Poggere et al., (2018), also found low magnetic signature on soil formed from tuffites in Brazilian soils with contrasting rock parent material.

The greater κ values on pyritized-andesites (**Fig. 4, table 3**), can be explained by the presence of pyrite and hydrothermal alteration process (Passier et al., 2001). Hydrothermal processes in island-arc settings, similar to the study area, can lead to the formation of hydrothermal magnetite. As hydrothermal fluids, heated by magmas, circulate through permeable rocks, they dissolve minerals and subsequently precipitate iron oxides, such as magnetite, in response to changes in fluid temperature, pressure, and chemistry (Nawrocki et al., 2021; Sillitoe, 2010). In addition, some of the elevated κ values may result from the formation of pyrite in pyritized andesites, along with the development of ferrimagnetic minerals such as pyrrhotite and magnetite within the rock (Figueiredo, 2000).

# 3.3 Ternary gamma-ray and magnetic susceptibility predicted maps, radionuclides content and $\kappa$ variability at landscape scale

The predicted maps of <sup>40</sup>K, eTh, and eU are demonstrated in figures 5A, 5B and 5C, respectively. In addition, figures 5D and 5E demonstrate the high resolution predicted ternary gamma-ray and magnetic susceptibility maps. Our initial focus lies on describing the interpretations of the three radionuclides in relation to the gamma-ray response associated to lithological-pedological substrates found in the specific landscapes and geomorphic processes.

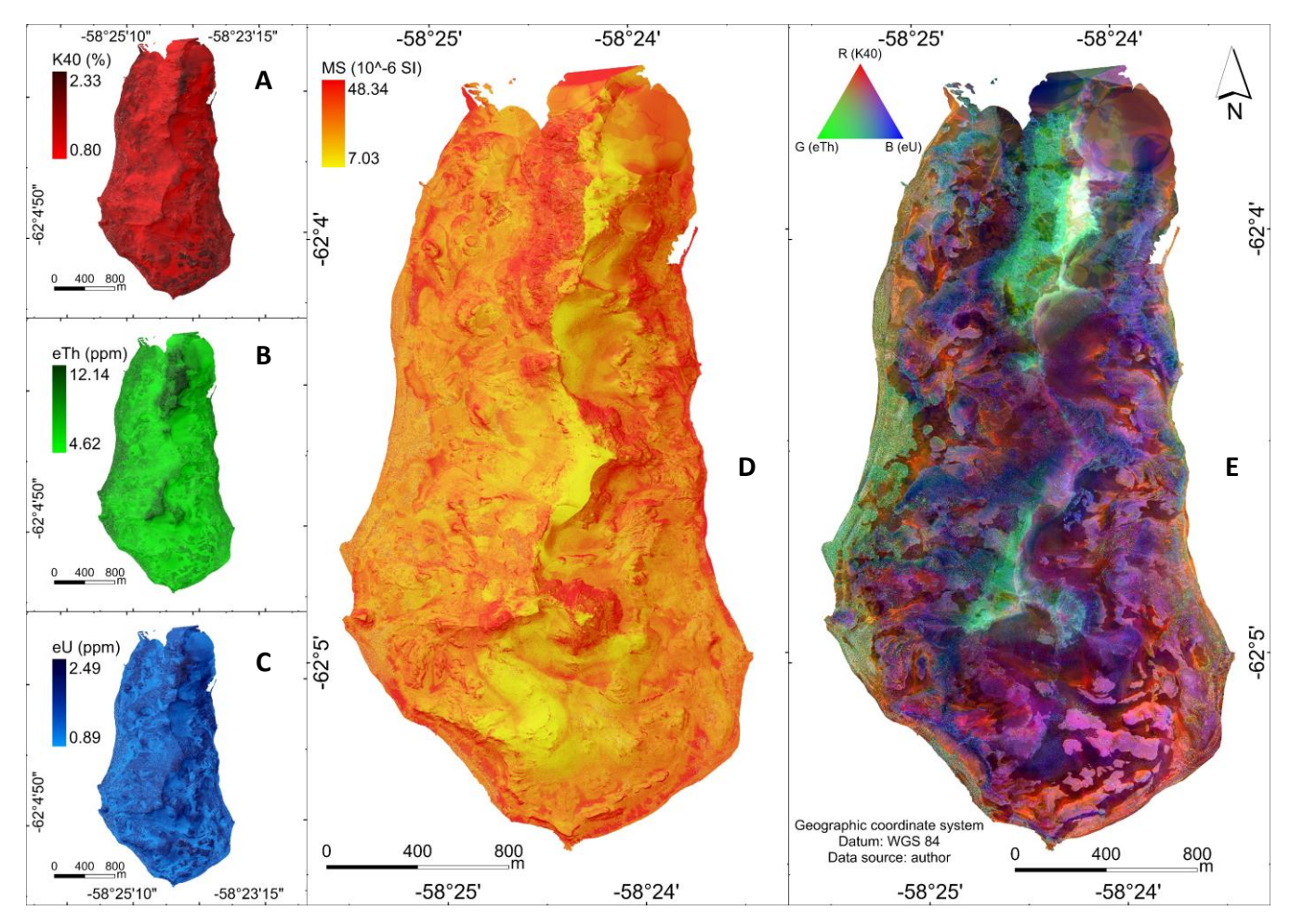


**Figure 5.** A) Predicted map of <sup>40</sup>K; B) Predicted map of eU; C) Predicted map of eTh; D) and E) 3D landscape perspective and magnetic susceptibility and gamma-ray ternary image, respectively over part of the Keller Peninsula. By integrating gamma-ray spectrometric images with digital elevation models (DEMs) in 3D perspective views, a comprehensive visualization emerges, revealing intricate connections between gamma-ray responses, terrain morphology attributes and surface processes (pedogeomorphological and periglacial).

425

430

435

The highest eTh values, predominantly represented by the green areas on the map, occur mainly over basaltic-andesite lithologies, rocks that are less mafic and richer in plagioclase and quartz (Fig. 5D). These regions coincide with flatter, high-elevation plateaus where deeper soils with higher clay content develop. The increased clay fraction enhances the adsorption capacity for eTh onto soil particle surfaces, thereby elevating eTh readings in these high plateau zones. In such areas, the spatial distribution and concentration of eTh are primarily controlled by lithology and pedogeomorphological factors.

In contrast, the western beach area, located at lower landscape positions, also exhibits elevated eTh levels associated with

undifferentiated sediments (Fig. 5E). This pattern is explained by the geomorphological setting where fluvioglacial meltwaters

originating from the high plateaus transport cryoclastically derived, eTh-rich sediments downslope. These sediments accumulate on the western beaches, demonstrating how erosive and depositional processes in a periglacial environment govern the distribution of eTh in this sector.

Regarding eU, the highest values are found on steep slopes characterized by shallow or absent soils, mainly over basaltic-andesites and andesitic-basalts lithologies (**Fig. 5E**). In these geomorphologically active areas, eU distribution largely reflects the chemical composition of the bedrock, indicating strong lithological and geomorphological control. Cryoclastically fractured and eroded materials are transported downslope by periglacial processes and deposited more evenly across lower plateaus, where eU concentrations reflect distinct source materials, in contrast to the focused sediment transport through fluvioglacial channels, which is responsible for eTh enrichment on the west beach. The <sup>40</sup>K values peaks predominantly in lower landscape positions, including lower plateaus and southeastern beaches, where andesitic-basalts and dioritic lithologies prevail (**Fig. 5E**). Conversely, pyritized-andesite zones show the lowest <sup>40</sup>K values, likely due to enhanced chemical weathering driven by natural acid drainage and sulfurization processes in local fluvioglacial channels. These processes accelerate potassium depletion, as observed in recent studies of sulfate-affected landscapes in Keller Peninsula (Mello et al., 2023). Therefore, both lithological composition and pedogeochemical processes regulate <sup>40</sup>K distribution in the area.

445

450

455

460

Previous research (Wilford and Minty, 2006; Dickson and Scott, 1997) has demonstrated that combining ternary gamma imaging with digital elevation models improves the interpretation of radionuclide spatial patterns by integrating lithological, soil, periglacial, and geomorphological influences (Mello et al., 2023b). Dickson and Scott (1997) showed that rock radioelement contents explain much of the gamma radiation variability, while also highlighting intra-class heterogeneity—granites, for example, lack a unique radionuclide signature. Similarly, Rawlins et al. (2012) quantified that bedrock type accounted for 52% of gamma radiation variability across Northern Ireland. Felsic rocks generally exhibit elevated eU, eTh, and <sup>40</sup>K contents (Rawlins et al., 2007). Recent tropical environment studies (Ribeiro et al., 2018; Souza et al., 2021; Guimarães et al., 2021; Mello et al., 2020, 2021, 2022a,b) have linked radionuclide variability to lithology in areas with minimal pedogenetic alteration, to relief in erosion and sediment deposition zones, and to weathering and pedogenesis in well-developed soils. However, recent studies, including the first applications of gamma spectrometry and magnetic susceptibility to Antarctic soils undertaken by (Mello et al., 2023; Mello et al., 2023), have suggested a strong influence of topography on the distribution of pedogeophysical variables, which were thoroughly detailed in this work.

Magnetic susceptibility (κ) values exhibit high spatial variability across lithologies, soils, and landforms, showing no consistent broad-scale pattern (Fig. 5D). Nonetheless, localized zones of elevated κ correlate with pyritized-andesite and andesitic-basalt lithologies, particularly on steep slopes or areas minimally influenced by sediment influx from other parts of the landscape. Conversely, hydrothermal alteration in pyritized andesites can enhance κ values as reported by Nawrocki et al., (2021) and Sillitoe, 2010). This effect is further intensified by higher iron availability and chemical weathering, which together concentrate ferrimagnetic minerals and contribute to increased susceptibility values (Figueiredo, 2000; Mello et al., 2023).

The lowest  $\kappa$  values are observed in areas dominated by Cryosols, which are young soils with minimal pedogenetic development (Fig. 5D). Although pedogenetic processes can influence  $\kappa$ , the low magnetic susceptibility primarily reflects the

lack of magnetite and other ferrimagnetic phases. The limited formation of secondary magnetic minerals appears less important for susceptibility differences than the accumulation of magnetite in more developed soils. This pattern aligns with findings by Daher et al. (2019), who reported low  $\kappa$  values in Antarctic soils derived from igneous rocks, attributed to their relatively young age and limited weathering.

475

480

485

490

495

500

505

The spatial distribution of radionuclides and magnetic susceptibility in Keller Peninsula (**Fig. 5**) results from a dynamic interplay between mineralogical characteristics of the bedrock, topographic controls on soil development and sediment transport, and active periglacial geomorphological processes. These factors collectively modulate the pedogeophysical signatures observed, producing patterns that cannot be solely attributed to lithology but rather to its modification through landscape evolution and pedogeochemical cycling.

Our results regarding the distribution of radionuclides across the landscape differ slightly from those commonly reported in the literature (Dickson and Scott, 1997; Mello et al., 2021; Wilford and Minty, 2006; Wilford and Thomas, 2012), which typically reports a strong correlation between radionuclide concentrations and the parent material in poorly developed soils. Although the low chemical weathering intensity observed in our study area suggests that lithology should exert primary control, the presence of highly dissected terrain, steep slopes, and active periglacial processes including periglacial erosion, freezingthawing cycles, and cryoturbation intensifies the influence of topography on the redistribution of radionuclides. As a result, in certain areas of Keller Peninsula, radionuclide concentrations in soils deviate from the expected values based solely on the underlying rock types. Practically all the relief variables are associated with the landform that control the surface periglacial and pedogeomorphological processes of the Keller Peninsula landscape. Periglacial erosion, glacial fluvial melt channels, freezing and thawing of the active layer of permafrost and solifluxion are the most frequent periglacial and pedogeomorphological processes in Keller Peninsula, as observed by Francelino et al., (2011) and López-Martínez et al., (2012). These processes promote the fragmentation, redistribution and mixing of materials in significant areas of the landscape (Mello et al., 2023; Mello et al., 2023), which can contribute to variations in radionuclide and k values, as well as increase prediction errors in the points of greater occurrence of these processes, such as the sloping areas of the landscape (Mello et al., 2022). The same periglacial processes and landscape dynamics also influence iron geochemistry. As a result, soils and areas underlain by mafic rocks such as basaltic-andesite and andesitic-basalt may exhibit relatively low concentrations of ferrimagnetic minerals, which is reflected in lower magnetic susceptibility readings (Fig. 4). The opposite can also occur; for example, soils developed over pyritized andesite show higher magnetic susceptibility values, indicating greater concentrations of ferrimagnetic minerals (Fig. 4).

The spatial patterns of natural radioactivity and magnetic susceptibility across Keller Peninsula are more strongly influenced by topography than by lithology. In steep, periglacially active terrains, geomorphic and pedogeomorphological processes such as cryoturbation, freeze—thaw cycles, and periglacial erosion promote the downslope transport and mixing of soil and minerals, resulting in the redistribution of radionuclides and ferrimagnetic minerals independent of bedrock type. Birkenmajer's (1980) geological mapping and petrographic studies further support that variations in mineral assemblages, especially between lightly altered mafic rocks and hydrothermal zones, and the presence of secondary minerals such as zeolites, albite, and iron oxides

contribute to these patterns. Consequently, pedogeophysical signals (e.g., eU, eTh, <sup>40</sup>K, and magnetic susceptibility) often reflect a mixed mineralogical signature redistributed by topographic and geomorphological dynamics, rather than a direct inheritance from the parent material. This may explain our observations such as unexpectedly low magnetic susceptibility over mafic rocks and elevated values over altered andesites, underscoring the dominant role of relief and periglacial processes in shaping pedogeophysical variability in Keller Peninsula.

### 3.3 Applicability of geophysical techniques on soil-lithological survey and understanding of periglacial processes

510

515

520

525

530

A relationship between radionuclide content/distribution and  $\kappa$  in the landscape in a digital elevation model are demonstrated in figures 6 and 7, respectively). Rock color variations between different lithologies were also observed in the field (**Fig. 8**). The content and distribution of radionuclides and  $\kappa$  are occasionally associated with the lithology of the area, making it difficult to establish a direct and generalist relationship between radionuclides and  $\kappa$  with the lithological units. This method allows for the estimation of apparent surface concentrations of naturally occurring radionuclides and their relationship with lithology, pedogeomorphological and periglacial processes (Mello et al., 2023b). By assuming that the absolute and relative concentrations of these radioelements vary significantly with lithology (Dickson and Scott, 1997; Wilford et al., 2016), gamma-ray spectrometric surveys can be used effectively for lithological mapping (Elawadi et al., 2004). However, in this particular study, the surface lithology is difficult to be map due to multiple geomorphological and periglacial processes that operates in M.A.

Gamma-ray ternary image combined with 3D landscape perspective in different views highlighting areas with higher and lower values of radionuclides (**Fig. 6**). The predicted ternary gamma-ray map (composite image) technique by machine learning was employed to simultaneously display three parameters of radioelement concentrations and distributions on a single image (**Fig. 6**). By utilizing color differences, this technique proved effective in discerning periglacial and pedogeomorphological processes associated to lithology and not only lithology (**Fig. 6**). This methodology allowed the identification of areas where distinct surface processes operate where different lithofacies occur within the larger mapped region and detailed studies involving surface process by using gamma-ray spectrometry and κ should be encouraged.

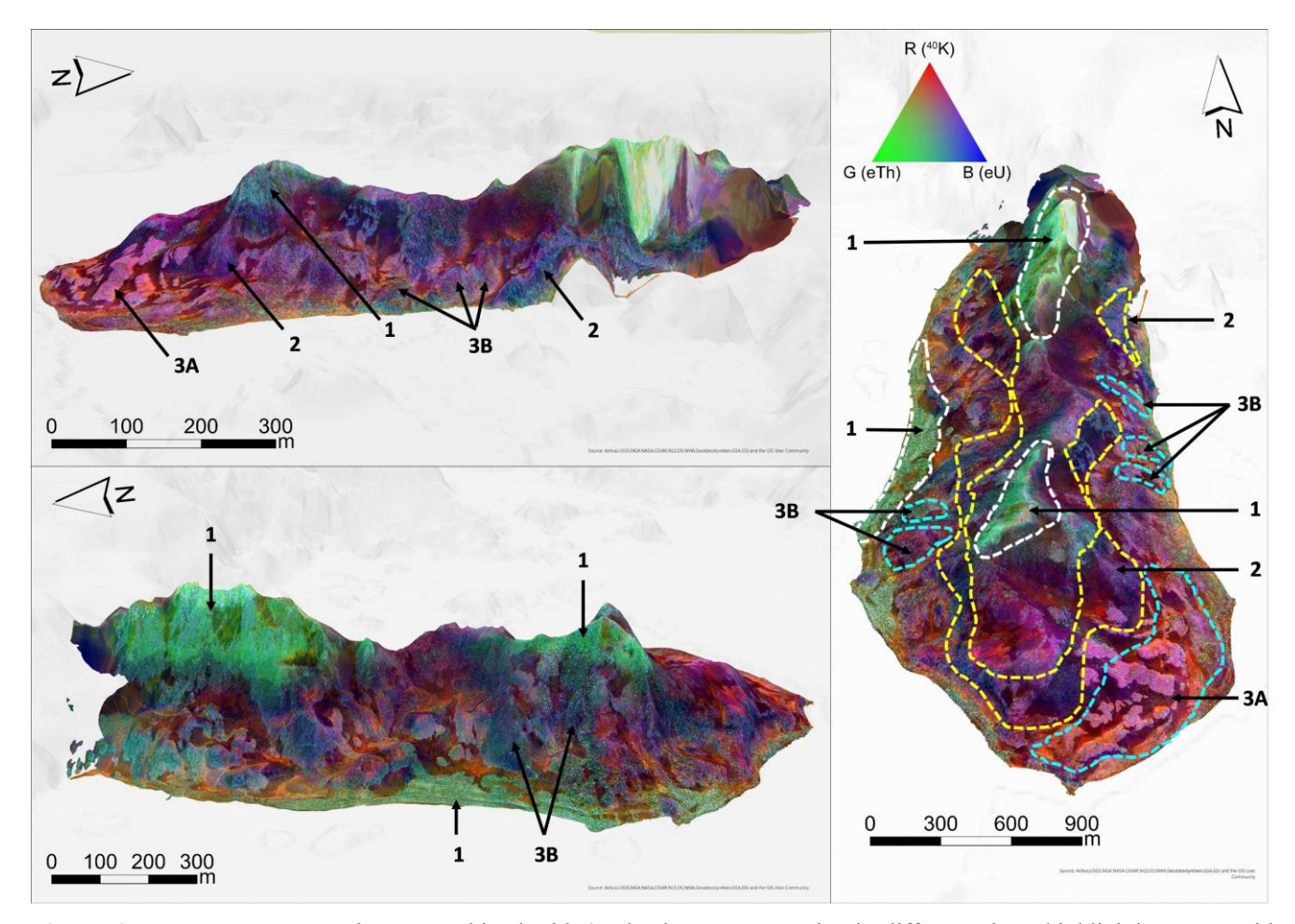


**Figure 6.** Gamma-ray ternary image combined with 3D landscape perspective in different views highlighting areas with higher and lower values of radionuclides. 1: higher eTh content; 2: higher eU content; 3A: higher <sup>40</sup>K content; 3B miner <sup>40</sup>K content in natural sulfate-affected areas.

535

540

Regarding  $\kappa$ , surface pedogeomorphological and periglacial processes also influence the distribution of magnetic susceptibility in the landscape, such that the spatial variability of  $\kappa$  has specific relationships with the lithology of the area (**Fig. 7**). Low values may not reflect the properties of the in-situ lithology, as many of the areas are affected by depositional processes caused by periglacial erosion, resulting in the mixing of surface materials (Mello et al., 2023). In a similar vein, Joju et al., (2023) conducted research and discovered that coarse soils in Larsemann Hills, East Antarctica, are primarily composed of magnetic minerals originating directly from the parent material, showcasing the strong influence of lithology on soil composition. Furthermore, despite the milder and moister climate in the maritime Antarctic region, Lee et al., (2004) observed minimal chemical weathering of bedrocks, suggesting that the soils mainly consist of physically weathered minerals and rock fragments.

Moreover, our findings align with those of Warrier et al., (2021a), who argued that while pedogenesis is indeed occurring, its intensity is insufficient to generate magnetic grains.

In some areas, the sulfurization due to hydrothermal processes, induced by the influence of pyritized-andesite (**Fig. 7**), leads to significant environmental acidification and hydrothermal magnetite formation affecting  $\kappa$  values (Souza et al., 2012; Lopes et al., 2019). This process may have played a role in the limited occurrence of ferrimagnetic minerals and their uniform distribution across the landscape contributing low variety in  $\kappa$  values (Mello et al., 2023b). Certain regions situated in the lower sections of the terrain are surrounded by mafic igneous rock (andesitic-basalts) in sloping areas, where periglacial erosion rates are high affect ferrimagnetic minerals distribution over landscape (Francelino et al., 2011; Mello et al., 2023) On the other hand, some areas are located on marine terraces composed of undifferentiated sediments, exhibiting diverse  $\kappa$  values patterns (Mello et al., 2023). The variation in  $\kappa$  values can be attributed to the presence of different sediment types with distinct mineralogical compositions in these specific locations.

550

555

560

565

It is also notable the occurrence of low  $\kappa$  values in the elevated and flat parts of the landscape (**Fig. 7**), where Cryosols occur. The permafrost in this compartment of the landscape hinders ferrimagnetic minerals formation. Water derived from snow melt during summer infiltrates through soil pores and accumulated in the active layer due to low permeability of permafrost. The saturation of soil induces gleyzation and avoid ferrimagnetic minerals precipitation (Zhu et al., 2021). In addition, the presence of a deeper regolith associated with periglacial processes of freezing and thawing of the active layer of permafrost, increases the differences between content and distribution of ferrimagnetic minerals on the surface and ferrimagnetic properties of the lithology (Mello et al., 2023).

The sensors were able to detect some lithological transitions, with significant changes in radionuclide and  $\kappa$  contents (**Fig. 8**). However, the sensors do not present values directly associated with lithology due to the high intensity of surface pedogeomorphological and periglacial processes, it exerts a great influence on pedogeophysical readings in agreement with Dickson and Scott, (1997); Mello et al., (2020) and Mello et al., (2021).

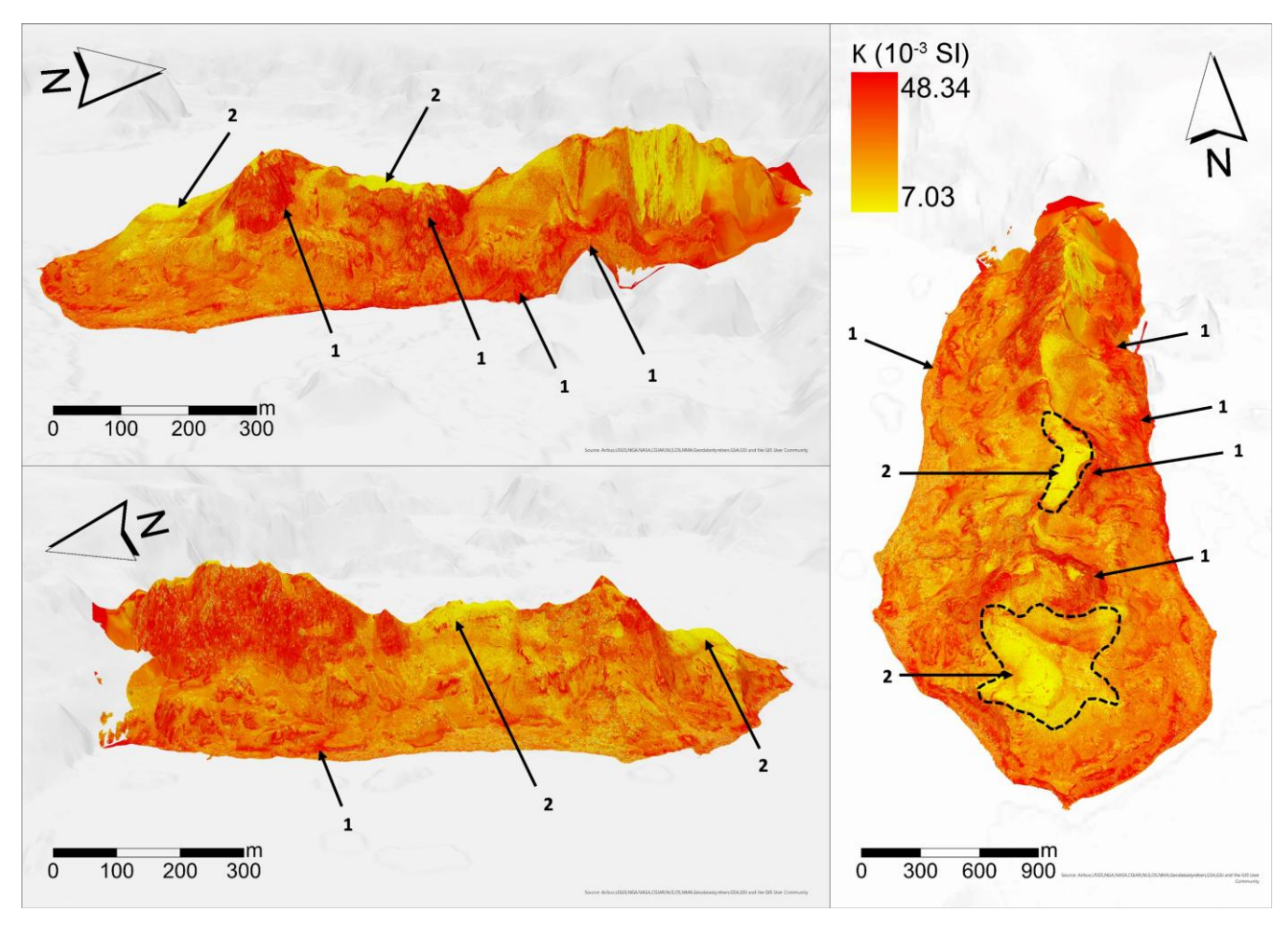


**Figure 7.** Magnetic susceptibility combined with 3D landscape perspective in different views highlighting areas with higher and lower  $\kappa$  values. 1: areas with high  $\kappa$  values; 2 areas with lower  $\kappa$  values over Cryosols.

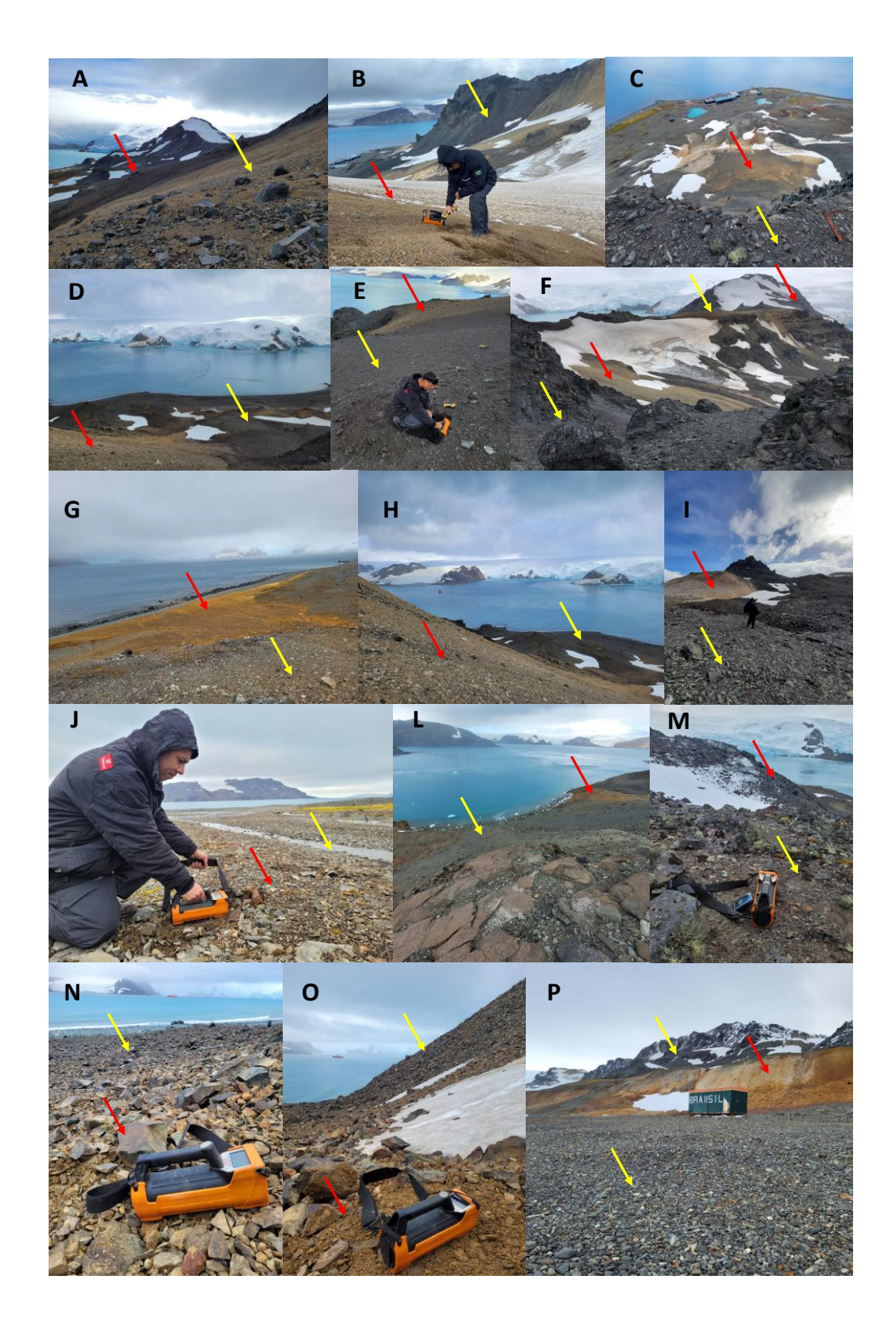


**Figure 8.** Examples of lithological transitions in Keller Peninsula. A: pyritized-andesite/ basaltic-andesites; B and C: pyritized-andesite/ andesitic-basalts; D and E: pyritized-andesite/ tuffites; F: pyritized-andesite/ andesitic-basalts; G: pyritized-andesite/basaltic-andesite/andesite/basaltic-andesite/diorite; J: undifferentiated marine sediments; L: tuffite/ pyritized-andesite; M: andesitic-basalts/ basaltic-andesites; N: undifferentiated marine sediments/pyritized-andesite; O: pyritized-andesite/ basaltic-andesites; P: andesitic-basalts/ pyritized-andesite/ undifferentiated marine sediments.

### 3.4 Study limitations and recommendations

Figure 9 demonstrates the coefficient of variation (prediction error) of the ternary gamma-ray and κ maps. The relatively low coefficient of variation values in our study can be attributed to the nested-LOOCV technique. These maps, associated with the CCC (table 2), illustrates the limitations of the models in predicting and spatializing pedogeophysical data. The prediction errors were low for the pedogeophysical variables, in agreement with the high CCC values shown in table 2, however, such errors do exist. It is possible to observe that the main prediction errors are associated with the steepest areas of the Peninsula, while the smallest are associated with areas with smoother to flat slopes. This shows that the main limitation of the modeling is related to the small number and distribution of samples read with the geophysical sensors. In this context, the relatively limited sample number as well as the distribution of samples is justified by the adverse field conditions (e.g., steep areas with snowbanks, glaciers, sharp rocks and frozen ground combined with high slopes, resulting in high danger areas for data acquisition by using proximal sensors). In other words, the logistical difficulties imposed by cold environments in field conditions were one of the significant limitations of this work, as noted by Fisher, (2014; 2015) and Mello et al., (2023). However, moderate CCC values and satisfactory CV in modeling processes, an exploratory evaluation for field data acquisition can provided informative results (Dharumarajan et al., 2017; Khaledian and Miller, 2020; Mansuy et al., 2014; Mosleh et al., 2016; Poggio et al., 2016).

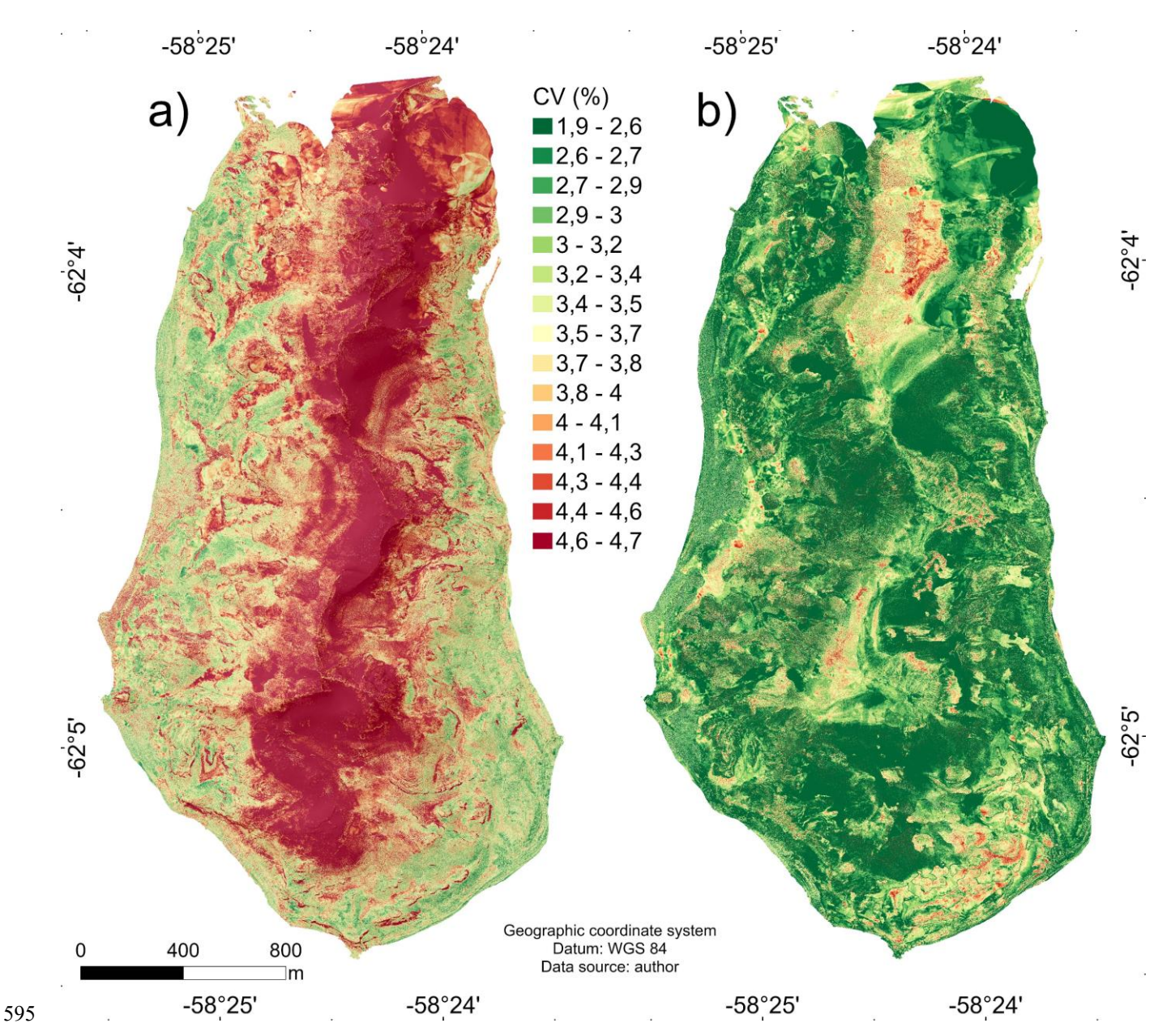


**Figure 9:** a) Coefficient of variation for magnetic susceptibility predicted map; b) Coefficient of variation for ternary gammaray predicted maps.

The low number of samples in this study (87) was not so appropriate for a more specific approach. However, the RF algorithm combined with nested-LOOCV were appropriate for small samples number, as demonstrated in other researches (Mello et al., 2022a; Mello et al., 2022b, 2022c). In addition, in-situ evaluation brings several uncontrolled factors (such as rocks or

fragments mixing due to periglacial erosion, permafrost activity, fluvioglacial channels and others), can impact the prediction and reduce the CCC and increase CV (Mello et al., 2023b).

The absence of detailed mineralogical, petrographic, and geochemical analyses constitutes a limitation of this study. This constraint was primarily due to logistical and operational challenges associated with fieldwork in remote and climatically extreme environments, which limited both the time available for sample collection and the transport of materials for laboratory analysis. Additionally, the main focus of the study was the application and evaluation of predictive models based on surface pedogeophysical data, rather than a comprehensive mineralogical-petrographic characterization. Nevertheless, we mitigated this limitation by incorporating and referencing existing detailed geological studies of the area, which provided essential information on the lithological framework, mineralogy and post-magmatic alteration processes. This information contributed significantly to understanding lithology as both a source of radionuclides and a provider of iron, which plays a key role in the formation of ferrimagnetic minerals either through pedogenetic processes (in the clay fraction) or as an inherited feature from the parent material (in the sand fraction). We recommend that future studies integrate in situ mineralogical and geochemical analyses to deepen the interpretation of the geophysical signals and refine model accuracy. Another limitation of this study is the unavailability of spatially continuous detailed lithological map (1:5000 for example), which affects the prediction performance (CCC, table 2) and CV maps (Fig. 9). Furthermore, the variability of sensor readings is another limitation, which is little, but it exists. As a result, this variability can reduce the accuracy of the information. Nevertheless, our methodology tackled this concern by extending the reading time of the gamma-ray sensor to 3 minutes and employing the mean values of three magnetic susceptibility readings. Mello et al., (2023), carried out a similar approach where the same errors and experimental conditions were observed when modeling the intensity of weathering and studying pedogenesis in soil profiles in Keller Peninsula, using machine learning algorithms. These researchers also adjusted the data collection method with the same geophysical sensors used in this research.

The applicability of the findings here, however, is restricted to comparable environments, specifically those exhibiting periglacial conditions, igneous lithology, similar precipitation, temperature, and relief patterns. Given that many of the Maritime Antarctica Islands and some parts of Antarctic Peninsula share these common or similar environmental features, it is strongly recommended to promote similar pedogeophysical survey characterization efforts.

### 4. Conclusion

605

610

615

620

625

630

635

The research introduced a structured approach to specialize pedogeophysical variables using machine learning techniques. It has been demonstrated that employing machine learning methodologies is promising for accurately mapping natural gammaray radioactivity and magnetic susceptibility characteristics. Through our methodology, we fitted regression models that identified key predictors, assessing accuracy and uncertainty across the RF model and ensuring consistent predictions through multiple pedogeoenvironmental iterations.

The RF algorithm was efficient and successfully predicted detailed maps of gamma-spectrometric and magnetic susceptibility variables in periglacial environments with diverse igneous rock substrates. Relief-related morphometric variables significantly

influenced the distribution of radionuclides and ferrimagnetic minerals on the land surface. The nested-LOOCV method proved suitable for pedogeophysical data with limited samples, providing robust evaluation of algorithm performance and generating accurate and high-performing mean maps.

Although the low degree of pedogenetic development and limited chemical weathering in the study area would typically suggest a strong lithological control over radionuclide concentrations, our findings indicate that topographic factors play a more dominant role. The highly dissected relief, steep slopes, and active periglacial processes, such as erosion and cryoturbation, contribute significantly to the redistribution of materials and radionuclides. As a result, in certain areas of Keller Peninsula, radionuclide concentrations do not align with the expected values based solely on the underlying lithology.

The highest levels of eTh were observed in three key areas: the elevated parts of the landscape, the flat areas, and the west beach. The west beach receives detrital materials from periglacial erosion, which come through fluvioglacial melting channels from the eTh-rich elevated parts. The eTh contents are controlled by lithology and pedogeomorphological processes.

The highest eU contents were observed in the steepest areas, characterized by the greatest slope, forming a ring around the highest parts of the landscape. In this case, the control of eU contents is determined by lithology and geomorphological processes, such as rock cryoclasty, periglacial erosion, and heterogeneous Accumulation of materials in the lower elevations of the terrain.

The highest levels of <sup>40</sup>K were found in the most felsic rocks and areas with minimal influence from material deposition caused by periglacial erosion. Conversely, the lowest contents of <sup>40</sup>K were observed in regions affected by the pedogeochemical process of sulfurization, specifically on pyritized-andesite within/around fluvioglacial melting channels. The control of <sup>40</sup>K levels is determined by both lithology and pedogeochemical processes.

The κ did not exhibit an apparent distribution pattern, although the highest levels were observed in pyritized-andesites areas, while the lowest levels were found in Cryosol areas. Pyritized andesites were influenced by hydrothermal alteration, where heat and magmatic fluids promoted iron concentration and the formation of hydrothermal magnetite, thereby contributing to higher κ values. On the other hand, Cryosols, in addition to increasing the distance between surface materials and the rocky substrate, experience seasonal freezing and thawing activity of the active permafrost layer, creating conditions that discourage the formation of ferrimagnetic minerals and reduce κ values. The control of κ values is determined by lithology and less influenced by pedological-periglacial processes associated with Cryosols.

In areas with diverse terrain attributes and a prevalence of active and intense periglacial processes, the predicted-spatialized pedogeophysical variables do not accurately represent the lithological composition of the substrate. This is because the various periglacial processes in the region, combined with the morphometric characteristics of the landscape, work to redistribute, mix, and homogenize the surface materials.

### 5. Acknowledgements

640

645

650

665

We express our gratitude to the National Council for Scientific and Technological Development (CNPq) for providing the first author's scholarship and essential resources through grant No. 134608/2015-1 and grant number 305996/2018-5. Additionally,

we acknowledge partial funding for this study from the Coordenação de Aperfeiçoamento de Pessoal de Nível Superior - Brazil (CAPES) - Finance Code 001.

We extend our thanks to the Terrantar – UFV group, Geotechnologies in Soil Science group, Laboratório de Geoprocessamento e Pedometria – UFV (LabGeo – UFV), 'Programa de Pós-Graduação em Solos e Nutrição de Plantas – PGSNP' of the Soil Department of the Universidade Federal de Viçosa, Brazil, and Programa Antártico Brasileiro for their valuable support.

675

# 6. Declaration of Generative AI and AI-assisted technologies in the writing process

Statement: During the preparation of this work, the authors utilized GPT-4 to correct the grammar and structure of the English language, ensuring clarity in the sentences for the reader. After using this tool/service, the author reviewed and edited the content as needed and take full responsibility for the content of the publication.

680

685

690

### 7. Code and data availability

All analyses and codes used in this research were developed in R software version 4.0.3 (R Core Team, 2023; Kuhn et al., 2013). The codes and data used in this research can be found at <a href="https://zenodo.org/doi/10.5281/zenodo.10828281">https://zenodo.10828281</a> (Moquedace et al., 2024). All packages used in the R software, as well as their respective versions, are listed in the database, and codes are available in the data base.zip file in the indicated repository.

# 8. Authors contribution

**Danilo César de Mello:** conceived of the presented idea, carried out the experiment, developed the theoretical formalism, contributed to the design and implementation of the research, to the analysis of the results and to the writing of the manuscript. He provided critical feedback and helped shape the research, analysis and manuscript.

Clara Glória Baldi: designed the model and the computational framework and analysed the data, planned and carried out the simulations, performed the analytic calculations and performed the numerical simulations, modelling processing, evaluate algorithms performance, variables importance and statistical analyses.

695

Cassio Marques Moquedace: contributed to the interpretation of the results, took the lead in writing the manuscript. Devised the project, the main conceptual ideas and proof outline. He worked out almost all of the technical details. All authors provided critical feedback and helped shape the research, analysis and manuscript.

700 Isabele de Angeli Oliveira: contributed to the interpretation of the results, took the lead in writing the manuscript. All authors provided critical feedback and helped shape the research, analysis and manuscript.

**Gustavo Vieira Veloso:** contributed to the interpretation of the results, took the lead in writing the manuscript. All authors provided critical feedback and helped shape the research, analysis and manuscript.

705

**Lucas Carvalho Gomes:** performed the analysis, drafted the manuscript and designed the figure. All authors provided critical feedback and helped shape the research, analysis and manuscript.

**Márcio Rocha Francelino:** Provided de financial support, leadership of the group, critical revision of the article. He contributed to the interpretation of the results and verified the analytical methods. Encouraged the co-authors to investigate a specific aspect and supervised the findings of this work.

Carlos Ernesto Gonçalves Reynaud Schaefer: Critical revision of the article. All authors discussed the results and commented on the manuscript. He contributed to the interpretation of the results and verified the analytical methods.

715

**Elpídio Inácio Fernandes Filho:** Critical revision of the article. He designed the model and the computational framework and analysed the data. He contributed to the interpretation of the results and verified the analytical methods. All authors discussed the results and commented on the manuscript.

José João Leal Lelis de Souza: Critical revision of the article. He contributed to the interpretation of the results and verified the analytical methods. All authors discussed the results and commented on the manuscript.

**Edgar Batista de Medeiros Júnior:** Critical revision of the article. He contributed to the interpretation of the results and verified the analytical methods. All authors discussed the results and commented on the manuscript.

725

**Fabio Soares de Oliveira:** Critical revision of the article. He contributed to the interpretation of the results and verified the analytical methods. All authors discussed the results and commented on the manuscript.

**Tiago Osório Ferreira:** Critical revision of the article. He contributed to the interpretation of the results and verified the analytical methods. All authors discussed the results and commented on the manuscript.

**José Alexandre Melo Demattê:** Critical revision of the article. He contributed to the interpretation of the results and verified the analytical methods. All authors discussed the results and commented on the manuscript.

# 735 9. Competing interests

The authors have the following competing interests: At least one of the (co-)authors is a member of the editorial board of Geoscientific Model Development.

### 10. References

- Arivazhagan, S., Naseer, K.A., Mahmoud, K.A., Arun Kumar, K. V, Libeesh, N.K., Sayyed, M.I., Alqahtani, M.S., Yousef, E.S., Khandaker, M.U., 2022. Gamma-ray protection capacity evaluation and satellite data-based mapping for the limestone, charnockite, and gneiss rocks in the Sirugudi taluk of the Dindigul district, India. Radiat. Phys. Chem. 196, 110108. https://doi.org/https://doi.org/10.1016/j.radphyschem.2022.110108
- Bastos, B.P., Pinheiro, H.S.K., Junior, W.C., dos Anjos, L.H.C., Ferreira, F.J.F., 2023. Clustering airborne gamma-ray spectrometry data in Nova Friburgo, State of Rio de Janeiro, southeastern Brazil. J. Appl. Geophys. 209, 104900. https://doi.org/https://doi.org/10.1016/j.jappgeo.2022.104900
  - Beamish, D., 2015. Relationships between gamma-ray attenuation and soils in SW England. Geoderma 259–260, 174–186. https://doi.org/10.1016/j.geoderma.2015.05.018
  - Beckett, P.H.T., 1971. Soil variability: a review. Soils Fertil. 34, 1–15.
- Polish Polar Res. 1, 29–54. Birkenmajer, K., 1980. Geology of Admiralty Bay, King George Island (South Shetland Islands)—An outline. Polish Polar Res. 1, 29–54.
  - Brenning, A., 2008. Statistical geocomputing combining R and SAGA: The example of landslide susceptibility analysis with generalized additive models. Hamburg. Beiträge zur Phys. Geogr. und Landschaftsökologie 19, 410.
  - Bressan, T.S., Kehl de Souza, M., Girelli, T.J., Junior, F.C., 2020. Evaluation of machine learning methods for lithology
- 755 classification using geophysical data. Comput. Geosci. 139, 104475. https://doi.org/https://doi.org/10.1016/j.cageo.2020.104475
  - Chen, D., Chang, N., Xiao, J., Zhou, Q., Wu, W., 2019. Mapping dynamics of soil organic matter in croplands with MODIS data and machine learning algorithms. Sci. Total Environ. 669, 844–855. https://doi.org/https://doi.org/10.1016/j.scitotenv.2019.03.151
- Chen, S., Liang, Z., Webster, R., Zhang, G., Zhou, Y., Teng, H., Hu, B., Arrouays, D., Shi, Z., 2019. A high-resolution map of soil pH in China made by hybrid modelling of sparse soil data and environmental covariates and its implications for pollution. Sci. Total Environ. 655, 273–283. https://doi.org/https://doi.org/10.1016/j.scitotenv.2018.11.230
  - Clevers, J.G.P.W., Van Der Heijden, G.W.A.M., Verzakov, S., Schaepman, M.E., 2007. Estimating grassland biomass using SVM band shaving of hyperspectral data. Photogramm. Eng. Remote Sensing 73, 1141–1148.
- 765 https://doi.org/10.14358/PERS.73.10.1141
  - Costa, I.S.L., Tavares, F.M., de Oliveira, J.K.M., 2019. Predictive lithological mapping through machine learning methods: a case study in the Cinzento Lineament, Carajás Province, Brazil. J. Geol. Surv. Brazil 2, 26–36.

- Cracknell, M.J., Reading, A.M., 2014. Geological mapping using remote sensing data: A comparison of five machine learning algorithms, their response to variations in the spatial distribution of training data and the use of explicit spatial information.
- 770 Comput. Geosci. 63, 22–33. https://doi.org/10.1016/j.cageo.2013.10.008

795

- Daher, M., Schaefer, C.E.G.R., Fernandes Filho, E.I., Francelino, M.R., Senra, E.O., 2019. Semi-arid soils from a topolithosequence at James Ross Island, Weddell Sea region, Antarctica: Chemistry, mineralogy, genesis and classification. Geomorphology 327, 351–364. https://doi.org/10.1016/j.geomorph.2018.11.003
  - de Mello, D.C., Ferreira, T.O., Veloso, G.V., de Lana, M.G., de Oliveira Mello, F.A., Di Raimo, L.A.D.L., Cabrero, D.R.O.,
- de Souza, J.J.L.L., Fernandes-Filho, E.I., Francelino, M.R., 2023. Digital mapping of soil weathering using field geophysical sensor data coupled with covariates and machine learning. J. South Am. Earth Sci. 104449.
  - de Souza, J.J.L.L., Schaefer, C.E.G.R., Abrahão, W.A.P., de Mello, J.W. V, Simas, F.N.B., da Silva, J., Francelino, M.R., 2012. Hydrogeochemistry of sulfate-affected landscapes in Keller Peninsula, Maritime Antarctica. Geomorphology 155, 55–61.
- 780 Dharumarajan, S., Hegde, R., Singh, S.K., 2017. Spatial prediction of major soil properties using Random Forest techniques -10, Α case study in semi-arid tropics of South India. Geoderma Reg. 154-162. https://doi.org/https://doi.org/10.1016/j.geodrs.2017.07.005
  - Dickson, B.L., Scott, K.M., 1997. Interpretation of aerial gamma-ray surveys adding the geochemical factors. AGSO J. Aust. Geol. Geophys. 17, 187–200.
- Dobos, E., 2003. The application of remote sensing and terrain modeling to soil characterization. Innov. Soil-Plant Syst. Sustain. Agric. Pract. 328–348.
  - e Souza, A.B., Demattê, J.A.M., Bellinaso, H., de Mello, D.C., da Silva Lisboa, C.J., de Oliveira Mello, F.A., Marques, K.P.P., de Resende, M.E.B., Reis, J.V., Mancini, M., 2021. A sensors-based profile heterogeneity index for soil characterization. Catena 207, 105670.
- Flawadi, E., Ammar, A., Elsirafy, A., 2004. Mapping surface geology using airborne gamma-ray spectrometric survey data-A case study, in: Proceedings of the 7th SEGJ International Symposium, Japan.
  - Fabris, J.D., Coey, J.M.D., Qi, Q., Mussel, W. da N., 1995. Characterization of Mg-rich maghemite from tuffite. Am. Mineral. 80, 664–669.
  - FAO, 2014. World reference base for soil resources 2014. International soil classification system for naming soils and creating
- Feng, Y., Cui, N., Hao, W., Gao, L., Gong, D., 2019. Estimation of soil temperature from meteorological data using different machine learning models. Geoderma 338, 67–77. https://doi.org/https://doi.org/10.1016/j.geoderma.2018.11.044
  - Ferreira, R.G., da Silva, D.D., Elesbon, A.A.A., Fernandes-Filho, E.I., Veloso, G.V., de Souza Fraga, M., Ferreira, L.B., 2021.
- Machine learning models for streamflow regionalization in a tropical watershed. J. Environ. Manage. 280, 111713.

legends for soil maps, World Soil Resources Reports No. 106. https://doi.org/10.1017/S0014479706394902

Ferreira, R.G., da Silva, D.D., Elesbon, A.A.A., Fernandes-Filho, E.I., Veloso, G.V., de Souza Fraga, M., Ferreira, L.B., 2020.

Machine learning models for streamflow regionalization in a tropical watershed. J. Environ. Manage. 111713.

- Figueiredo, B.R., 2000. Minérios e ambiente. Editora da UNICAMP.
- Fisher, M., 2015. A Day in the Life of an Arctic Soil Scientist. Soil Horizons 56, 1–3.
- Fisher, M., 2014. The Challenges of Doing Soils Research in Antarctica: A Day in the Life of Ed Gregorich. Soil Horizons 55,
- 805 1–3.
  - Ford, K., Harris, J.R., Shives, R., Carson, J., Buckle, J., 2008. Remote predictive mapping 2. Gamma-ray spectrometry: A tool for mapping Canada's North. Geosci. Canada 35, 109–126.
  - Francelino, M.R., Schaefer, C.E.G.R., Simas, F.N.B., Fernandes Filho, E.I., de Souza, J.J.L.L., da Costa, L.M., 2011. Geomorphology and soils distribution under paraglacial conditions in an ice-free area of Admiralty Bay, King George Island,
- 810 Antarctica. Catena 85, 194–204.
  - French, H.M., 2017. The periglacial environment. John Wiley & Sons.
  - Garankina, E. V, Lobkov, V.A., Shorkunov, I.G., Belyaev, V.R., 2022. Identifying relict periglacial features in watershed landscape and deposits of Borisoglebsk Upland, Central European Russia. J. Geol. Soc. London.
  - Gregory, A.F., Horwood, J.L., 1961. A laboratory study of gamma-ray spectra at the surface of rocks. Geological Survey of
- 815 Canada, Ottawa, (Canada). Dept. of Mines and Technical ....
  - Guimarães, C.C.B., Dematte, J.A.M., de Azevedo, A.C., Dalmolin, R.S.D., ten Caten, A., Sayão, V.M., da Silva, R.C., Poppiel, R.R., de Sousa Mendes, W., Salazar, D.F.U., 2021. Soil weathering behavior assessed by combined spectral ranges: Insights into aggregate analysis. Geoderma 402, 115154.
  - Harris, J.R., Grunsky, E.C., 2015. Predictive lithological mapping of Canada's North using Random Forest classification
- 820 applied to geophysical and geochemical data. Comput. Geosci. 80, 9–25. https://doi.org/https://doi.org/10.1016/j.cageo.2015.03.013
  - Henderson, B.L., Bui, E.N., Moran, C.J., Simon, D.A.P., 2005. Australia-wide predictions of soil properties using decision trees. Geoderma 124, 383–398. https://doi.org/https://doi.org/10.1016/j.geoderma.2004.06.007
  - Hijmans, R.J., Van Etten, J., 2016. raster: Geographic Data Analysis and Modeling. R package version 2.5-8.
- Honeyborne, I., McHugh, T.D., Kuittinen, I., Cichonska, A., Evangelopoulos, D., Ronacher, K., van Helden, P.D., Gillespie, S.H., Fernandez-Reyes, D., Walzl, G., Rousu, J., Butcher, P.D., Waddell, S.J., 2016. Profiling persistent tubercule bacilli from patient sputa during therapy predicts early drug efficacy. BMC Med. 14, 1–13. https://doi.org/10.1186/s12916-016-0609-3 Hothorn, T., 2021. CRAN task view: Machine learning & statistical learning.
  - INPE, 2009. Instituto Nacional de Pesquisas Espaciais [WWW Document].

accurate uncertainty propagation. Struct. Multidiscip. Optim. 1–19.

- Joju, G.S., Warrier, A.K., Chaparro, M.A.E., Mahesh, B.S., Matthew, F.A., Anusree, S., Mohan, R., 2023. Mineral magnetic properties of surface soils from the broknes and Grovnes Peninsula, Larsemann Hills, East Antarctica. Polar Sci. 100968.
  Jung, Y., Lee, J., Lee, M., Kang, N., Lee, I., 2020. Probabilistic analytical target cascading using kernel density estimation for
  - Khaledian, Y., Miller, B.A., 2020. Selecting appropriate machine learning methods for digital soil mapping. Appl. Math.
- 835 Model. 81, 401–418.

- Khosravi, V., Doulati Ardejani, F., Yousefi, S., Aryafar, A., 2018. Monitoring soil lead and zinc contents via combination of spectroscopy with extreme learning machine and other data mining methods. Geoderma 318, 29–41. https://doi.org/10.1016/j.geoderma.2017.12.025
- Kuhn, M., Johnson, K., 2013. Applied predictive modeling. Springer.
- Kuhn, M., Wing, J., Weston, S., Williams, A., Keefer, C., Engelhardt, A., Cooper, T., Mayer, Z., Kenkel, B., Team, R.C., 2020. Package 'caret.' R J.
  - Kuhn, S., Cracknell, M.J., Reading, A.M., 2018. Lithologic mapping using Random Forests applied to geophysical and remote-sensing data: A demonstration study from the Eastern Goldfields of Australia. Geophysics 83, B183–B193.
  - Lee, Y. Il, Lim, H.S., Yoon, H. Il, 2004. Geochemistry of soils of King George Island, South Shetland Islands, West Antarctica:
- 845 Implications for pedogenesis in cold polar regions. Geochim. Cosmochim. Acta 68, 4319–4333. https://doi.org/https://doi.org/10.1016/j.gca.2004.01.020
  - Lin, L.I.-K., 1989. A Concordance Correlation Coefficient to Evaluate Reproducibility. Biometrics 45, 255–268. https://doi.org/10.2307/2532051
- Loiseau, T., Richer-de-Forges, A.C., Martelet, G., Bialkowski, A., Nehlig, P., Arrouays, D., 2020. Could airborne gamma-spectrometric data replace lithological maps as co-variates for digital soil mapping of topsoil particle-size distribution? A case study in Western France. Geoderma Reg. 22, e00295. https://doi.org/https://doi.org/10.1016/j.geodrs.2020.e00295
  - Lopes, D., Schaefer, C.E.G.R., Souza, J.J.L.L. de, Oliveira, F.S. de, Simas, F.N.B., Daher, M., Gjorup, D.F., 2019. Concretionary horizons, unusual pedogenetic processes and features of sulfate affected soils from Antarctica. Geoderma 347, 13–24. https://doi.org/https://doi.org/10.1016/j.geoderma.2019.03.024
- 855 López-Martínez, J., Serrano, E., Schmid, T., Mink, S., Linés, C., 2012. Periglacial processes and landforms in the South Shetland Islands (northern Antarctic Peninsula region). Geomorphology 155–156, 62–79. https://doi.org/https://doi.org/10.1016/j.geomorph.2011.12.018
  - Malone, B.P., McBratney, A.B., Minasny, B., Laslett, G.M., 2009. Mapping continuous depth functions of soil carbon storage and available water capacity. Geoderma 154, 138–152. https://doi.org/10.1016/j.geoderma.2009.10.007
- Mansuy, N., Thiffault, E., Paré, D., Bernier, P., Guindon, L., Villemaire, P., Poirier, V., Beaudoin, A., 2014. Digital mapping of soil properties in Canadian managed forests at 250m of resolution using the k-nearest neighbor method. Geoderma 235–236, 59–73. https://doi.org/https://doi.org/10.1016/j.geoderma.2014.06.032
  - Meier, M., Francelino, M.R., Gasparini, A.S., Thomazini, A., Pereira, A.B., von Krüger, F.L., Fernandes-Filho, E.I., Schaefer, C.E.G.R., 2023. Soilscapes and geoenvironments at Stansbury Peninsula, Nelson Island, maritime Antarctica. CATENA 223,
- 865 106884. https://doi.org/https://doi.org/10.1016/j.catena.2022.106884
  - Mello, D., Alexandre Melo Demattê, J., Alexandra de Oliveira Mello, F., Roberto Poppiel, R., ElizabetQuiñonez Silvero, N., Lucas Safanelli, J., Barros e Souza, A., Augusto Di Loreto Di Raimo, L., Rizzo, R., Eduarda Bispo Resende, M., Ernesto Gonçalves Reynaud Schaefer, C., 2021. Applied gamma-ray spectrometry for evaluating tropical soil processes and attributes. Geoderma 381. https://doi.org/10.1016/j.geoderma.2020.114736

- Mello, D., Demattê, J.A.M., Silvero, N.E.Q., Di Raimo, L.A.D.L., Poppiel, R.R., Mello, F.A.O., Souza, A.B., Safanelli, J.L., Resende, M.E.B., Rizzo, R., 2020. Soil magnetic susceptibility and its relationship with naturally occurring processes and soil attributes in pedosphere, in a tropical environment. Geoderma 372. https://doi.org/10.1016/j.geoderma.2020.114364
  Mello, Danilo, Demattê, J.A.M., Silvero, N.E.Q., Di Raimo, L.A.D.L., Poppiel, R.R., Mello, F.A.O., Souza, A.B., Safanelli, J.L., Resende, M.E.B., Rizzo, R., 2020. Soil magnetic susceptibility and its relationship with naturally occurring processes and
- https://doi.org/10.1016/j.geoderma.2020.114364

  Mello, D.C., Ferreira, T.O., Veloso, G.V., de Lana, M.G., de Oliveira Mello, F.A., Di Raimo, L.A.D.L., Schaefer, C.E.G.R., Francelino, M.R., Fernandes-Filho, E.I., Demattê, J.A.M., 2022a. Pedogenetic processes operating at different intensities inferred by geophysical sensors and machine learning algorithms. CATENA 216, 106370.

tropical

environment.

Geoderma

372,

114364.

875

soil

attributes

in

pedosphere,

in

- Mello, D.C., Safanelli, J.L., Poppiel, R.R., Veloso, G.V., Cabrero, D.R.O., Greschuk, L.T., Mello, F.A. de O., Francelino, M.R., Ker, J.C., Leite, E.P., 2022b. Soil apparent electrical conductivity survey in different pedoenvironments by geophysical sensor EM38: a potential tool in pedology and pedometry studies. Geocarto Int. 1–24.
  - Mello, D.C., Veloso, G.V., Moquedace, C.M., de Angeli Oliveira, I., de Oliveira, F.S., Gomes, L.C., de Souza, J.J.L.L., Francelino, M.R., Fernandes-Filho, E.I., Schaefer, C.E.G.R., Demattê, J.A.M., 2023a. Radiometric and magnetic susceptibility
- characterization of soil profiles: Geophysical data and their relationship with Antarctic periglacial processes, pedogenesis, and lithology. CATENA 232, 107427. https://doi.org/https://doi.org/10.1016/j.catena.2023.107427
   Mello, D.C., Vieira, G., Marques, C., Angeli, I. De, Soares, F., Oliveira, D., Demattê, M., 2023b. Chemical weathering
  - detection in the periglacial landscapes of Maritime Antarctica: New approach using geophysical sensors, topographic variables and machine learning algorithms 438. https://doi.org/10.1016/j.geoderma.2023.116615
- Mello, D.C. de, Ferreira, T.O., Veloso, G.V., Lana, M.G. de, Mello, F.A. de O., Di Raimo, L.A.D.L., Cabrero, D.R.O., Souza, J.J.L.L. de, Fernandes-Filho, E.I., Francelino, M.R., 2022a. Weathering intensities in tropical soils evaluated by machine learning, clusterization and geophysical sensors. SOIL Discuss. 1–41.
  - Mello, D.C., Veloso, G.V., Moquedace, C.M., de Angeli Oliveira, I., de Oliveira, F.S., Gomes, L.C., de Souza, J.J.L.L., Francelino, M.R., Fernandes-Filho, E.I., Schaefer, C.E.G.R., Demattê, J.A.M., 2023. Radiometric and magnetic susceptibility
- characterization of soil profiles: Geophysical data and their relationship with Antarctic periglacial processes, pedogenesis, and lithology. CATENA 232, 107427. https://doi.org/https://doi.org/10.1016/j.catena.2023.107427
  - Mello, D.C., Safanelli, J.L., Poppiel, R.R., Veloso, G.V., Cabrero, D.R.O., Greschuk, L.T., de Oliveira Mello, F.A., Francelino, M.R., Ker, J.C., Leite, E.P., 2022b. Soil apparent electrical conductivity survey in different pedoenvironments by geophysical sensor EM38: a potential tool in pedology and pedometry studies. Geocarto Int. 1–22.
- Mello, D.C. de, Veloso, G.V., Mello, M.F. de, Lana, M.G. de, Oliveira, I. de A., Mello, F.A. de O., Siqueira, R.G., Gomes, L.C., Fernandes-Filho, E.I., Schaefer, C.E.G.R., Francelino, M.R., Leite, E.P., Ferreira, T.O., Demattê, J.A.M., 2025. Integrating proximal geophysical sensing and machine learning for digital soil mapping: Spatial prediction and model evaluation using a small dataset. Soil Adv. 3, 100024. https://doi.org/https://doi.org/10.1016/j.soilad.2024.100024

- Mello, D.C. de, Veloso, G.V., Lana, M.G. de, Mello, F.A. de O., Poppiel, R.R., Cabrero, D.R.O., Di Raimo, L.A.D.L.,
  Schaefer, C.E.G.R., Leite, E.P., Demattê, J.A.M., 2022c. A new methodological framework for geophysical sensor combinations associated with machine learning algorithms to understand soil attributes. Geosci. Model Dev. 15, 1219–1246.
  Minty, B.R.S., 1988. A Review of Airborne Gamma-Ray Spectrometric Data-Processing Techniques. Aust. Gov. Publ. Serv. Mishra, G., Sulieman, M.M., Kaya, F., Francaviglia, R., Keshavarzi, A., Bakhshandeh, E., Loum, M., Jangir, A., Ahmed, I., Elmobarak, A., Basher, A., Rawat, D., 2022. Machine learning for cation exchange capacity prediction in different land uses.
- Oatena 216, 106404. https://doi.org/https://doi.org/10.1016/j.catena.2022.106404
  Mosleh, Z., Salehi, M.H., Jafari, A., Borujeni, I.E., Mehnatkesh, A., 2016. The effectiveness of digital soil mapping to predict soil properties over low-relief areas. Environ. Monit. Assess. 188, 195.
  Mullins, C.E., 1977. Magnetic Susceptibility of the Soil and Its Significance in Soil Science a Review. J. Soil Sci. 28, 223–246. https://doi.org/10.1111/j.1365-2389.1977.tb02232.x
- Navas, A., Serrano, E., López-Martínez, J., Gaspar, L., Lizaga, I., 2018. Interpreting environmental changes from radionuclides and soil characteristics in different landform contexts of Elephant Island (maritime Antarctica). L. Degrad. Dev. 29, 3141– 3158.

- Nawrocki J., Pańczyk M., Wójcik K. And Tatura. 2021. U-Pb isotopic ages and provenance of some far-travelled exotic pebbles from glaciogenic sediments of the Polonez Cove Formation (Oligocene, King George Island). Journal of Geological Society, London 178: igs2020-113.
- Nawrocki, J., Pańczyk, M., Kozłowska-Roman, A., 2021. Age of volcanism on Keller Peninsula and assessment of age-constrained volcanic activity on King George Island, West Antarctica. Polish Polar Res. 77–95.
- Neogi, S., Dauwels, J., 2019. Factored Latent-Dynamic Conditional Random Fields for Single and Multi-label Sequence Modeling. arXiv Prepr. arXiv1911.03667.
- Paes, É. de C., Veloso, G.V., Fonseca, A.A. da, Fernandes-Filho, E.I., Fontes, M.P.F., Soares, E.M.B., 2022. Predictive modeling of contents of potentially toxic elements using morphometric data, proximal sensing, and chemical and physical properties of soils under mining influence. Sci. Total Environ. 817, 152972. https://doi.org/https://doi.org/10.1016/j.scitotenv.2022.152972
- Passier, H.F. d, De Lange, G.J., Dekkers, M.J., 2001. Magnetic properties and geochemistry of the active oxidation front and the youngest sapropel in the eastern Mediterranean Sea. Geophys. J. Int. 145, 604–614.
  - Poggere, G.C., Inda, A.V., Barrón, V., Kämpf, N., de Brito, A.D.B., Barbosa, J.Z., Curi, N., 2018. Maghemite quantification and magnetic signature of Brazilian soils with contrasting parent materials. Appl. Clay Sci. https://doi.org/10.1016/j.clay.2018.05.014
  - Poggio, L., Gimona, A., Spezia, L., Brewer, M.J., 2016. Bayesian spatial modelling of soil properties and their uncertainty:
- 935 The example of soil organic matter in Scotland using R-INLA. Geoderma 277, 69–82. https://doi.org/https://doi.org/10.1016/j.geoderma.2016.04.026
  - Pollard, W., 2018. Periglacial processes in glacial environments, in: Past Glacial Environments. Elsevier, pp. 537–564.

- Pride, D.E., Cox, C.A., Moody, S. V, Conelea, R.R., Rosen, M.A., 1990. Investigation of mineralization in the South Shetland Islands, Gerlache Strait, and Anvers Island, northern Antarctic Peninsula. Miner. Resour. Potential Antarct. 51, 69–94.
- 940 R Core Team, 2023. R: A language and environment for statistical computing.
  - Ragland, P.C., Billings, G.K., Adams, J.A.S., 1967. Chemical fractionation and its relationship to the distribution of thorium and uranium in a zoned granite batholith. Geochim. Cosmochim. Acta 31, 17–33. https://doi.org/https://doi.org/10.1016/0016-7037(67)90095-6
  - Rakusa-Suszczewski, S., Mietus, M., Piasecki, J., 1993. Weather and climate. Marit. Antarct. Coast. Ecosyst. Admir. Bay.
- 945 Warsaw Polish Acad. Sci. 19–25.
  - Rawlins, B.G., Lark, R.M., Webster, R., 2007. Understanding airborne radiometric survey signals across part of eastern England. Earth Surf. Process. Landforms 32, 1503–1515, https://doi.org/10.1002/esp.1468
  - Rawlins, B.G., Scheib, C., Tyler, A.N., Beamish, D., 2012. Optimal mapping of terrestrial gamma dose rates using geological parent material and aerogeophysical survey data. J. Environ. Monit. 14, 3086–3093.
- Ribeiro, F.C.A., Silva, J.I.R., Lima, E.S.A., do Amaral Sobrinho, N.M.B., Perez, D. V., Lauria, D.C., 2018. Natural radioactivity in soils of the state of Rio de Janeiro (Brazil): Radiological characterization and relationships to geological formation, soil types and soil properties. J. Environ. Radioact. 182, 34–43. https://doi.org/10.1016/j.jenvrad.2017.11.017

  Rytky, S.J.O., Tiulpin, A., Frondelius, T., Finnilä, M.A.J., Karhula, S.S., Leino, J., Pritzker, K.P.H., Valkealahti, M., Lehenkari, P., Joukainen, A., Kröger, H., Nieminen, H.J., Saarakkala, S., 2020. Automating three-dimensional osteoarthritis
- histopathological grading of human osteochondral tissue using machine learning on contrast-enhanced micro-computed tomography. Osteoarthr. Cartil. 28, 1133–1144. https://doi.org/10.1016/j.joca.2020.05.002
  - Sales, S. and C., 2021. Terraplus KT-10 v2 User Manual.
  - Sarmast, M., Farpoor, M.H., Esfandiarpour Boroujeni, I., 2017. Magnetic susceptibility of soils along a lithotoposequence in southeast Iran. Catena 156, 252–262. https://doi.org/10.1016/j.catena.2017.04.019
- 960 Schünemann, A.L., Almeida, P.H.A., Thomazini, A., Fernandes Filho, E.I., Francelino, M.R., Schaefer, C.E.G.R., Pereira, A.B., 2018. High-resolution topography for Digital Terrain Model (DTM) in Keller Peninsula, Maritime Antarctica. An. Acad. Bras. Cienc. 90, 2001–2010.
  - Schwertmann, U., 1988. Occurrence and formation of iron oxides in various pedoenvironments, in: Iron in Soils and Clay Minerals. Springer, pp. 267–308.
- Shebl, A., Abdellatif, M., Hissen, M., Ibrahim Abdelaziz, M., Csámer, Á., 2021. Lithological mapping enhancement by integrating Sentinel 2 and gamma-ray data utilizing support vector machine: A case study from Egypt. Int. J. Appl. Earth Obs. Geoinf. 105, 102619. https://doi.org/10.1016/j.jag.2021.102619.
  - Siqueira, R.G., Moquedace, C.M., Francelino, M.R., Schaefer, C.E.G.R., Fernandes-Filho, E.I., 2023. Machine learning applied for Antarctic soil mapping: Spatial prediction of soil texture for Maritime Antarctica and Northern Antarctic Peninsula.
- 970 Geoderma 432, 116405. https://doi.org/https://doi.org/10.1016/j.geoderma.2023.116405.
  - Sillitoe, R.H., 2010. Porphyry copper systems. Econ. Geol. 105, 3–41.

- Siqueira, R.G., Veloso, G. V, Fernandes-Filho, E.I., Francelino, M.R., Schaefer, C.E.G.R., Correa, G.R., 2022. Evaluation of machine learning algorithms to classify and map landforms in Antarctica. Earth Surf. Process. Landforms 47, 367–382.
- Sisson, T.W., Grove, T.L., 1993. Experimental investigations of the role of H2O in calc-alkaline differentiation and subduction
- 975 zone magmatism. Contrib. to Mineral. Petrol. 113, 143–166. https://doi.org/10.1007/BF00283225
  - Svensson, D.N., Messing, I., Barron, J., 2022. An investigation in laser diffraction soil particle size distribution analysis to obtain compatible results with sieve and pipette method. Soil Tillage Res. 223, 105450.
  - Taylor, M.J., Smettem, K., Pracilio, G., Verboom, W., 2002. Relationships between soil properties and high-resolution radiometrics, central eastern Wheatbelt, Western Australia. Explor. Geophys. 33, 95–102.
- Turner, J., Colwell, S.R., Marshall, G.J., Lachlan-Cope, T.A., Carleton, A.M., Jones, P.D., Lagun, V., Reid, P.A., Iagovkina, S., 2005. Antarctic climate change during the last 50 years. Int. J. Climatol. 25, 279–294.
  - Turner, J., Overland, J.E., Walsh, J.E., 2007. An Arctic and Antarctic perspective on recent climate change. Int. J. Climatol. A J. R. Meteorol. Soc. 27, 277–293.
  - Vingiani, S., Agrillo, A., De Mascellis, R., Langella, G., Manna, P., Mileti, F.A., Terribile, F., 2022. Multi-Sensor Approach
- Ombined with Pedological Investigations to Understand Site-Specific Variability of Soil Properties and Potentially Toxic Elements (PTEs) Content of an Industrial Contaminated Area. Appl. Sci. https://doi.org/10.3390/app12083993
  - Viscarra Rossel, R. A. (2011). Fine-resolution multiscale mapping of clay minerals in Australian soils measured with near infrared spectra. *Journal of Geophysical Research: Earth Surface*, 116(F4).
- Warrier, A.K., Mahesh, B.S., Sebastian, J.G., Mohan, R., 2021. How strong was pedogenesis in Schirmacher Oasis during the
- 990 Late Quaternary? Polar Sci. 30, 100636. https://doi.org/https://doi.org/10.1016/j.polar.2021.100636
  Whitfield, J.M., Rogers, J.J.W., Adams, J.A.S., 1959. The relationship between the petrology and the thorium and uranium contents of some granitic rocks. Geochim. Cosmochim. Acta 17, 248–271. https://doi.org/https://doi.org/10.1016/0016-
- Wilford, J., Minty, B., 2006. Chapter 16 The Use of Airborne Gamma-ray Imagery for Mapping Soils and Understanding Landscape Processes. Dev. Soil Sci. 31. https://doi.org/10.1016/S0166-2481(06)31016-1
  - Wilford, J.R., Searle, R., Thomas, M., Pagendam, D., Grundy, M.J., 2016. A regolith depth map of the Australian continent. Geoderma 266, 1–13. https://doi.org/10.1016/j.geoderma.2015.11.033
  - Wilford, P.N., Bierwirth, J.R., Craig, M.A., 1997a. and Applied Geomorphology 17.

7037(59)90099-7

- Wilford, P.N., Bierwirth, J.R., Craig, M.A., 1997b. Application of airborne gamma-ray spectrometry in soiVregolith mapping and Applied Geomorphology 17.
  - Zhao, X., Zhao, D., Wang, J., Triantafilis, J., 2022. Soil organic carbon (SOC) prediction in Australian sugarcane fields using Vis–NIR spectroscopy with different model setting approaches. Geoderma Reg. 30, e00566.
  - Zhou, Y., Zhao, X., Guo, X., Li, Y., 2022. Mapping of soil organic carbon using machine learning models: Combination of optical and radar remote sensing data. Soil Sci. Soc. Am. J. 86, 293–310.

Zhu, C., Wang, H., Li, S., Luo, Y., Xue, T., Song, Y., Qiu, A., Liu, H., 2021. Mineral magnetism variables as potential indicators of permafrost aggradation and degradation at the southern edge of the permafrost zone, Northeast China. Boreas 50, 497–518.